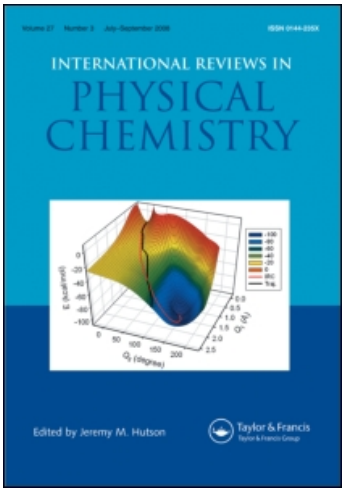

International Reviews in Physical Chemistry
Publication details, including instructions for authors and subscription information:
http://www.informaworld.com/smpp/title~content=t713724383

The time-dependent quantum wave packet approach to the electronically nonadiabatic processes in chemical reactions

Tian-Shu Chu[a]; Yan Zhang[a]; Ke-Li Han[a]
[a] State Key Laboratory of Molecular Reaction Dynamics, Chinese Academy of Sciences, Dalian Institute of Chemical Physics, Dalian 116023, China

Online publication date: 28 November 2010

To cite this Article Chu, Tian-Shu , Zhang, Yan and Han, Ke-Li(2006) 'The time-dependent quantum wave packet approach to the electronically nonadiabatic processes in chemical reactions', International Reviews in Physical Chemistry, 25: 1, 201 — 235
To link to this Article: DOI: 10.1080/01442350600677929
URL: http://dx.doi.org/10.1080/01442350600677929

International Reviews in Physical Chemistry,
Vol. 25, Nos. 1–2, January–June 2006, 201–235

Taylor & Francis
Taylor & Francis Group

The time-dependent quantum wave packet approach to the electronically nonadiabatic processes in chemical reactions

TIAN-SHU CHU, YAN ZHANG and KE-LI HAN*

State Key Laboratory of Molecular Reaction Dynamics,
Dalian Institute of Chemical Physics, Chinese Academy of Sciences, Dalian 116023, China

(*Received 20 January 2006; in final form 4 March 2006*)

The time-dependent quantum wave packet approach has been improved and formulated to treat the multiple surface problems and thus provided a new simple, yet a clear quantum picture for interpreting the reaction mechanism underlying the nonadiabatic dynamical processes. The method keeps the salient feature of the original quantum wave packet theory developed for single surface problems, i.e. the introduction of the absorbing potential and the grid basis including the discrete variable representation and the fast Fourier transformation, which makes the present methodology a very efficient implement for the nonadiabatic quantum scattering calculations. Here, we review the theoretical basis of this approach and its applications to the fundamental triatomic chemical reactions, the latter include the nonadiabatic dynamics calculations on the $F+H_2$, $F+HD$, $F+D_2$, $O(^1D)+N_2$, $O(^3P, {}^1D)+H_2$, D^++H_2, and H^++D_2 reactions. We also present a thorough historical overview of the theoretically nonadiabatic dynamical investigations particularly on the triatomic systems, and show how the time-dependent wave packet approach complements the time-independent quantum scattering theory.

Contents

*Corresponding author. Email: klhan@dicp.ac.cn

International Reviews in Physical Chemistry
ISSN 0144–235X print/ISSN 1366–591X online © 2006 Taylor & Francis
http://www.tandf.co.uk/journals
DOI: 10.1080/01442350600677929

1. Introduction

Tremendous advances in computer science as well as in electronic structure theory have stimulated the recent theoretical interest in explaining the various aspects of the electronically nonadiabatic processes in chemical reactions [1–3]. On the theoretical side, the nonadiabatic dynamical investigation has now evolved to a stage where the exact quantum scattering calculation has finally been achieved for a few benchmark triatomic systems. Going beyond the triatomic systems and more towards the complicated polyatomic systems, however, remains a formidable challenge to exact quantum dynamics. The dynamical treatment of the polyatomic reactions [4–6] will therefore necessarily turn to the semiclassical mechanical approach at the present stage; and to this end, various theoretical approaches have been developed thus far to treat the chemical reactions with nonadiabatic effects. These included the Tully's fewest switches (TFS) [7, 8], the fewest switches with time-uncertainty (FSTU) [9, 10], the exact complete passage (ECP) [11], the semiclassical Ehrenfest (SE) [12], the coherent switching decay of mixing (CSDM) [13], the full multiple spawning (FMS) [14, 15], the multi-configuration time-dependent Hartree (MCTDH) [16, 17] methods, etc. Coupled with the quantum features, the semiclassical treatment of the reaction system indeed provides a pragmatic way for simulating the nonadiabatic processes both in the triatomic and the polyatomic reactions. But for interpreting the reaction mechanism underlying the nonadiabatic processes occurring in triatomic system, the full quantum dynamical treatment is much more easy to implement, and is therefore preferable to the semiclassical mechanical methods. Although the quantum dynamics has now reached a point where the multiple surface problem has been recently solved without any approximation for a few benchmark abstraction reactions by time-independent approach, the complexity of quantum scattering calculations involving a large number of electronic states, as well as the diversity in chemical reactions still offer us the opportunity to apply different theoretical methodologies for exploring the dynamical information related to the electronically nonadiabatic processes.

The challenge associated with the nonadiabatic quantum scattering calculations lies in that the equation of motion should be formulated within a basis set of electronic wave functions since more than one electronic state is involved in the overall dynamics.

As a result, the number of the basis functions used in expanding the wave function of the system increases rapidly with the inclusion of the internal rovibrational basis functions for each electronic state, thus making the quantum scattering calculations intractable. The use of a high-speed computer and a parallel computation may alternatively provide a solution to this problem, but the essential way lies still in developing new dynamical methods that require less computational resources. The time-dependent quantum wave packet approach [18–24] seems to serve this purpose, because it is well acknowledged from the adiabatic scattering calculations that the time-dependent wave packet approach has advantages over the time-independent quantum method, in that, its computational cost scales with less than N^2 as compared with the latter one with N^3; here N is the number of basis functions. The time-dependent wave packet approach takes advantage of the fast Fourier transformation and the discrete variable representation that was introduced to evaluate the action of the Hamiltonian onto the wave function, as well as the absorbing potential to reduce the spatial extent of the grid. Hence, it is usually numerically more efficient to solve the Schrödinger equation using the wave packet method. However, to date, the applications of the time-dependent wave packet method to the chemical reactions have successfully revealed their adiabatic dynamical features only. It was therefore realised that an improvement should be made to this method, for the purpose of using it as an efficient computational tool to handle the nonadiabatic dynamical issues. For this reason, the time-dependent wave packet method has been introduced to treat the nonadiabatic dynamics of chemical reactions, and has been developed from the one within the framework of the Born-Oppenheimer approximation [19] into an appropriate approach to solve the Schrödinger equation formulated with the augment of electronic basis. It is also worth noting that an accurate *ab initio* description of the potential energy surfaces and the nonadiabatic coupling terms is clearly essential in any dynamical calculation.

In this review, we shall explore the uses and advantages of this time-dependent quantum wave packet approach in the area of nonadiabatic quantum scattering calculations. After a historical overview on the advances made in the previous theoretically nonadiabatic treatments for the triatomic chemical reactions in section 2, section 3 introduces the theoretical framework of the time-dependent wave packet method for nonadiabatically investigating the triatomic systems. The applications of this method to benchmark reactions $F(^2P_{3/2},^2P_{1/2}) + H_2$, $F(^2P_{3/2},^2P_{1/2}) + HD$, and $F(^2P_{3/2},^2P_{1/2}) + D_2$, to the electronic quenching process of $O(^1D) + N_2$, to the spin–orbit-induced intersystem crossing effects in $O(^3P,^1D) + H_2$, and to the charge transfer processes in $D^+ + H_2$ and $H^+ + D_2$ are presented in section 4. These quantum results demonstrate the dynamical phenomena of the chemical processes which occur in the triatomic systems either with barriers or with potential wells, and provide physical insights into the reaction mechanisms. Finally, section 5 concludes with a suggestion for future developments of the method.

2. Historical overview

One of the most widely investigated reactions is the abstraction reaction $F(^2P_{3/2},^2P_{1/2}) + H_2$ in which the ground state $1^2A'$ and the excited state $1^2A''$ correlate

adiabatically with the ground spin state $F(^2P_{3/2})$, while the excited state $2^2A'$ correlates with the excited spin state $F(^2P_{1/2})$. Triggered by the pioneering work of Tully [25], there are extensive theoretical reports [26–33] on the role of the excited spin state and nonadiabatic effects in this reaction, of which the time-independent quantum dynamical approach by Alexander *et al*. [30, 31] has yielded the recent success in providing the exact and the accurate scattering calculations. They included into the Hamiltonian the electronic (spin and orbital) angular momenta of the F atom to describe the electronic motion with an exact treatment of their operation on the multi-state wave function. They also recently fitted the diabatic potential energy surfaces and the spin–orbit coupling matrix which were used in the quantum scattering calculations carried out within the uncoupled electronic basis [31]. These elaborate nonadiabatic quantum calculations of Alexander *et al*. [30, 31] have revealed that the F atom in the excited spin state contributes little to the overall reactivity, with its contribution being clearly observed in the formation of product HF in the $v = 3$ vibrational level [34, 35], and the fine structure of the reaction probabilities and the integral cross sections is insensitive to the nonadiabatic effects. In addition, the agreement between the state-to-state calculations and the experimentally measured angular distributions for $F + H_2$ [36], and between the relative cross section and the experimental excited functions for the $F + HD$ [34] reaction has been revealed by these exact quantum studies. With a similar approach, Alexander *et al*. [37–40] also extended their nonadiabatic studies to the $Cl(^2P_{3/2},^2P_{1/2}) + H_2$ and $O(^1D) + H_2$ reactions very recently. They found that except for the spin–orbit coupling, the other coupling terms play insignificant roles in the reaction dynamics of $Cl(^2P_{3/2},^2P_{1/2}) + H_2$, and the discrepancy between the calculated differential cross section and the experimental measurement implies some defects in the exit channel of the ClHH PES. Combined with a capture theory, their calculated fine-structure branching ratio of the product OH in the $O(^1D) + H_2$ reaction with four electronic states involved in the dynamics, revealed a propensity for the formation of product OH in Π (Λ doublet) state and a statistical distribution of the cross sections over the final-state rotational quantum number. Similar to the $F + H_2$ reaction, the role of the excited state and spin–orbit coupling in the $Cl + H_2$ reaction has also been investigated by Skouteris *et al*. [41] and by Xie *et al*. [42]. Furthermore, Skouteris *et al*. [41] performed the time-dependent quantum scattering calculations for $Cl + H_2$ by using the Chebyshev iteration [43].

$Cl(^2P_{3/2},^2P_{1/2}) + HCl$ reaction also attracted lots of theoretical attentions. Schatz and coworkers [44, 46] have fitted the diabatic potential energy surfaces of this system to *ab initio* data calculated at two different levels, the higher one of which is RCCSD-T/aug-VTZ. They then performed the time-independent quantum scattering calculations within hyperspherical coordinates on these potential surfaces, together with the electrostatic, Coriolis, spin–orbit couplings, to obtain the cumulative reaction probability, the J-shift rate constant for total angular momentum $J = 1/2$. Recently, they investigated the influence of the spin–orbit coupling on the reaction dynamics via varying the spin–orbit coupling between -150 to 150% of the true Cl value in the time-independent quantum scattering calculations, as well as the influence of the van der Waals wells on the cumulative reaction probability and the fine-structure-resolved cumulative reaction probability by performing a $J = 1/2$ quantum scattering calculation [47, 48]. A thorough investigation on the $O(^1D) + H_2$ reaction has also been conducted

by Schatz and coworkers [49–53]. They employed various theoretical approaches such as the TFS method, the approximated quantum theory, and the helicity decoupled wave packet method in the nonadiabatic calculations performed on different potential energy surfaces, including their own constructed potential energy surface of the excited state 1A″, the diatomics-in-molecules (DIM) potential energy surface, and the accurate *ab initio* Dobbyn–Knowles (DK) potential energy surface. The physical insights into the role of the excited states 1A″ and 2A′, and the comparison between the estimated total reaction cross sections and the experimental data are therefore provided. The reaction probabilities of this reaction and its isotopic reactions $O(^1D) + HD/D_2$ have also been calculated on the same DK potential energy surface in the time-independent quantum study of Takayanagi [54]. Based on the analytical spin–orbit coupling matrix fitted to the calculated data using the Breit-Pauli method, Schatz and co-workers [55–57] also carried out, for the first time, the theoretical studies of intersystem crossing effects in the $O(^3P,^1D) + H_2$, $S(^3P,^1D) + H_2$ reactions by using trajectory surface hopping (TSH) method within a mixed representation. They calculated the fine-structure-resolved branching ratio and the product rotational distributions. The nonadiabatic studies of Schatz *et al*. [58, 59] still include the investigations on the Renner-Teller effects in the $N(^2D) + H_2$ reaction and on the reactive and the nonreactive quenching in the OH + H system [60].

Another reaction that has long been of interest to this field is the reaction of H_3^+ system. Its simplicity and yet rich reaction variety involving the charge transfer processes, has made the reaction and its isotopic variants the paradigms for a full quantum treatment. As early as 1972, Tully *et al*. [61] reported a TSH study of $H^+ + D_2$ reaction. Nakamura and co-workers [62–64] calculated the cumulative reaction probability for the total angular momentum $J = 0$ of $(D + H_2)^+$ reaction using both the TSH method based on the developed Zhu–Nakamura theory and the time-independent quantum scattering theory, and Takayanagi *et al*. [65] performed similar scattering calculations for this reaction system. The reaction probability for collinear reaction $(H + H_2)^+$ was calculated by Ushakov *et al*. [66] also using the time-independent quantum theory and the DIM potential matrix. Ichihara *et al*. [67] reported the reaction cross sections at low collision energy for the $H^+ + H_2$ reaction while Chajia *et al*. [68] investigated the collisions of H^+ with D_2 and with H_2 at low energies using the FMS method. The H_3^+ system was also subjected to the TSH study of Ichihara *et al*. [69]. In addition, there are many other theoretical nonadiabatic studies such as the TSH and the time-independent quantum scattering calculations on the electronic quenching process of $O(^1D)+N_2$ [70–72], the time-independent quantum scattering calculations on $Br(^2P_{1/2}) + H_2$ [73], the TSH studies of the charge transfer processes in $(Ar + H_2)^+$ [74, 75], and the TSH studies of C + CH [76], $Na + N_2$ [77] etc.

As should already be apparent from the above overview, most of the theoretically nonadiabatic treatments were carried out within either time-independent framework or semiclassical framework – this is in sharp contrast to the dynamics studies of adiabatic problems where the time-independent and the time-dependent quantum scattering theories give almost the same contribution and are complementary to each other. Therefore, the extension of the time-dependent quantum wave packet theory to the nonadiabatic dynamics is to be of fundamental importance for the development of dynamics methods in this exciting field.

3. Time-dependent quantum wave packet approach for A + BC reaction

We have used the time-dependent wave packet approach in which the split-operator scheme [78] is employed to numerically solve the Schrödinger equation for a reaction system based on the reactant Jacobi coordinates. The multi-state wave function is expanded within an electronic-translational-vibrational-rotational basis set. The starting point for the numerical solution is to construct the initial wave function that is to be propagated on a specific electronic state. Since the fundamental lines of the method could be found in [19, 20], here we only emphasise on those details associating with the treatment of the multiple electronic states.

3.1. *Propagation of the wave function*

To numerically solve the Schrödinger equation for a triatomic reaction system that is formulated within a basis set of electronic wave functions, the split-operator scheme [78] has been modified and then used for treating the propagation of the wave functions on several potential energy surfaces associated with the multiple electronic states. In terms of the reactant Jacobi coordinates, the time-dependent Schrödinger equation within a diabatic electronic basis for A + BC reaction system involving the multiple electronic states can be written as

$$\begin{aligned} i\hbar\frac{\partial}{\partial t}\Psi &= H\Psi \\ H &= -\frac{\hbar^2}{2\mu_R}\frac{\partial^2}{\partial R^2} - \frac{\hbar^2}{2\mu_r}\frac{\partial^2}{\partial r^2} + V(r) + \frac{\hat{j}^2}{2\mu_r r^2} + \frac{\hat{L}^2}{2\mu_R R^2} + V \end{aligned} \tag{3.1.1}$$

with $R(r)$ being the distance between atom A and the center of the mass of molecule BC (the distance between atom B and C), and $\mu_R(\mu_r)$the corresponding reduced mass, $V(r)$ is the reference diatomic vibrational potential, and $\boldsymbol{j}$ and $\boldsymbol{L}$ is the rotational and the orbital angular momentum respectively.

The wave function Ψ is a column vector,

$$\Psi = \begin{bmatrix} \Psi_1 \\ \Psi_2 \\ \cdots \\ \Psi_m \end{bmatrix} \tag{3.1.2}$$

with Ψ_i being the expansion coefficient obtained by expanding the multi-state wave function Ψ_{multi} in a diabatic electronic basis $\{\phi_i\}$ $(i = 1, m)$ [79],

$$\Psi_{\text{multi}} = \sum_i \Psi_i \phi_i \tag{3.1.3}$$

In fact, Ψ_i describes the nuclear motion in the ith electronic state, and is therefore further expanded in terms of a translational-vibrational-(body-fixed)

rotational basis set [19],

$$\Psi_i = \sum_{nvjk} F_{nvjk,i} u_n^v(R)\phi_v(r)\,Y_{jk}(R,r) \tag{3.1.4}$$

n, v, $j(k)$ labels the translational basis, the vibrational basis, and the rotational basis respectively.

V denotes the matrix representation of the potential energy in the diabatic electronic basis,

$$V = \begin{bmatrix} V_{11} & V_{12} & \dots & \dots & V_{1m} \\ V_{21} & V_{22} & \dots & \dots & V_{2m} \\ \dots & \dots & \dots & \dots & \dots \\ \dots & \dots & \dots & \dots & \dots \\ V_{m1} & V_{m2} & \dots & \dots & V_{mm} \end{bmatrix} \tag{3.1.5}$$

in which the diagonal elements $V_{ii} = \langle\phi_i|H_{\mathrm{el}}|\phi_i\rangle$ define the diabatic potential energy surfaces for each electronic state, and the off-diagonal elements $V_{ij} = \langle\phi_i|H_{\mathrm{el}}|\phi_j\rangle$ are generally non-zero, here, H_{el} is the electronic Hamiltonian.

The Schrödinger equation (3.1.1) can be numerically solved through the time propagation of the wave function by applying a modified split-operator scheme. For a short time step Δ in the propagation, the wave function at time $t+\Delta$ can be derived from $\Psi(t)$ as follows,

$$\begin{aligned} \Psi(t+\Delta) &= e^{-iH_0\Delta/2}e^{-iV_{\mathrm{rot}}\Delta/2}e^{-iV\Delta}e^{-iV_{\mathrm{rot}}\Delta/2}e^{-iH_0\Delta/2}\Psi(t) \\ &= e^{-iH_0\Delta/2}e^{-iV_{\mathrm{rot}}\Delta/2}Te^{-iV_{\mathrm{diag}}\Delta}T^{+}e^{-iV_{\mathrm{rot}}\Delta/2}e^{-iH_0\Delta/2}\Psi(t) \\ &= e^{-iH_0\Delta/2}e^{-iV_{\mathrm{rot}}\Delta/2}TET^{+}e^{-iV_{\mathrm{rot}}\Delta/2}e^{-iH_0\Delta/2}\Psi(t), \end{aligned} \tag{3.1.6}$$

with H_0 and V_{rot} being defined as,

$$\begin{aligned} H_0 &= -\frac{\hbar^2}{2\mu_R}\frac{\partial^2}{\partial R^2} - \frac{\hbar^2}{2\mu_r}\frac{\partial^2}{\partial r^2} + V(r) \\ V_{\mathrm{rot}} &= \frac{\hat{j}^2}{2\mu_r r^2} + \frac{\hat{L}^2}{2\mu_R R^2}, \end{aligned} \tag{3.1.7}$$

and V_{diag} is the diagonal matrix of V,

$$V_{\mathrm{diag}} = \begin{bmatrix} V_1 & 0 & 0 & \dots & 0 \\ 0 & V_2 & 0 & \dots & 0 \\ 0 & 0 & V_3 & \dots & 0 \\ \dots & \dots & \dots & \dots & 0 \\ 0 & 0 & 0 & \dots & V_m \end{bmatrix} \tag{3.1.8}$$

Here, T denotes the transformation matrix from matrix V to V_{diag}, and T^+ the conjugated transposed matrix of T. E also represents the diagonal matrix composed of the exponential functions as follows,

$$E = \begin{bmatrix} e^{-iV_1\Delta} & 0 & 0 & \dots & 0 \\ 0 & e^{-iV_2\Delta} & 0 & \dots & 0 \\ 0 & 0 & e^{-iV_3\Delta} & \dots & 0 \\ \dots & \dots & \dots & \dots & 0 \\ 0 & \dots & \dots & 0 & e^{-iV_m\Delta} \end{bmatrix} \tag{3.1.9}$$

Further, it is clear that the inclusion of the electronic angular momenta $\hat{l}$ and $\hat{s}$ in the orbital angular momentum $\hat{L}$ will cause the changes in the projection quantum numbers λ, σ of $\hat{l}$ and $\hat{s}$ while they are acting onto the electronic wave function. Hence, during the propagation of the wave function, the action of the centrifugal potential operator $\hat{L}^2/(2\mu_R R^2)$ should be first onto the electronic basis and then onto the nuclear wave function, leading to the changes in all projection quantum numbers K, k, λ, σ of $\hat{J}$, $\hat{j}$, $\hat{l}$ and $\hat{s}$, with $K = k + \lambda + \sigma$. For a detailed description of the action of $\hat{L}^2 = (\hat{J} - \hat{j} - \hat{l} - \hat{s})^2$ onto the wave function with both the electronic and the nuclear parts, the reader is refered to [31].

To save the computational cost, the Coriolis coupling is often neglected which is the case in the centrifugal sudden (CS) approximation. Within the CS approximation, the action of $\hat{L}^2$ onto the wave function can be simplified to (here we use $|Kk\lambda\sigma\rangle$ to denote the wave function for simplicity)

$$\hat{L}^2|Kk\lambda\sigma\rangle = [J(J+1) + j(j+1) + l(l+1) + s(s+1) - 2K^2 + 2k(\lambda+\sigma) + 2\lambda\sigma]|Kk\lambda\sigma\rangle \tag{3.1.10}$$

Otherwise, if the Coriolis coupling is included in the calculation, then such treatment is called the coupled-channel (CC) calculation.

3.2. *Preparation of the initial wave function*

For a specific electronic state j on which the initial wave packet is to be propagated, the corresponding wave function is chosen as a product of a specific rovibrational wave function and a localised translational wave packet expressed in a standard Gaussian function [19, 20] while being zero for the remaining electronic states,

$$\Psi_i(t=0) = \begin{cases} \varphi_{\bar{k},i}(R)\phi_{v_0 j_0,i}(r)\, Y_{j_0 k_0,i}(\hat{R},\hat{r}) & (i=j) \\ 0 & (i \neq j) \end{cases} \tag{3.2.1}$$

where $\phi_{v_0 j_0,i}(r)$ is the rovibrational function with respect to the initial rovibrational state v_0, j_0, and is expanded in the vibrational basis $\{\phi_v(r)\}$. $Y_{j_0 k_0,i}(\hat{R},\hat{r})$ represents the rotational function corresponding to the initial rotational state of j_0, k_0. $\varphi_{\bar{k},i}(R)$ denotes

the Gaussian function with an average momentum $\bar{k}$ and the wave packet width δ,

$$\varphi_{\bar{k},i}(R) = \left(\frac{1}{\pi\delta^2}\right)^{1/4} \exp(-(R-R_0)^2/2\delta^2)e^{-i\bar{k}R} \tag{3.2.2}$$

In addition, if we further consider that the diagonal form of the wave function can only be achieved within a coupled electronic basis $|jj_\alpha>$ ($\hat{j} = \hat{l} + \hat{s}$, $j_\alpha = \lambda + \sigma$), hence, if the quantum scattering calculations are performed within an uncoupled electronic basis $|l\lambda s\sigma>$, it is necessary to transform the above constructed initial wave function with a diagonal form in the coupled electronic basis to its corresponding form in the uncoupled electronic basis before the wave packet propagation. Such transformation can be obtained via the following Clebsch–Gordan (CG) transformation [44],

$$|\lambda\sigma> = \sum_{jj_\alpha} <jj_\alpha|l\lambda s\sigma> |jj_\alpha> \tag{3.2.3}$$

i.e. the wave functions expressed in the two different electronic basis sets are connected by the CG coefficients $<jj_\alpha|l\lambda s\sigma>$.

3.3. *Analysis of the final wave function*

Having propagated for a sufficiently longer time, we can now derive the time-independent wave function from the time-dependent final wave function by the following transformation from time-domain to the energy domain [19] (here, we omit the subscript i for simplicity),

$$\begin{aligned} \left|\Psi^+(E)\right\rangle &= \frac{1}{a(E)}\int_0^\infty e^{(i/\hbar)Et}\left|\Psi(t)\right\rangle dt \\ a(E) &= \left\langle\Psi^+(E)\mid\Psi(0)\right\rangle = \left\langle\Phi_E\mid\Psi(0)\right\rangle \end{aligned} \tag{3.3.1}$$

where Φ_E is a sine function and a Ricatti-Bessel function for zero and nonzero partial wave function, respectively.

The reaction probability in the reactive scattering calculation can be obtained by performing the flux calculation at a fixed surface $r = r_s$. For each electronic state i, the following formula is used to calculate the reaction probability,

$$\begin{aligned} P^R_{v_0j_0k_0,i}(E) &= \frac{\hbar}{\mu_r}\mathrm{Im}\left(\sum_{nvjkv'}\bar{F}^*_{nvjk,i}(E)\phi^*_v(r)\times\frac{\partial}{\partial r}\phi_{v'}(r)\bar{F}_{nv'jk,i}(E)\right)_{r=r_s} \\ \bar{F}_{nvjk,i}(E) &= \frac{1}{a(E)}\int_0^\infty e^{(i/\hbar)Et}\bar{F}_{nvjk,i}(t)dt \\ \bar{F}_{nvjk,i}(t) &= \sum_l A_{n,l}F_{lvjk,i}(t) \end{aligned} \tag{3.3.2}$$

with $A_{n,l}$ being the transformation matrix between the basis and the discrete variable representations along the R-direction. Here, v_0, j_0 is the initial vibrational and

rotational quantum number of the diatomic molecule, and k_0 is the projection quantum number of j_0.

However, in nonreactive scattering calculation, the probability correlating to the electronic state i can be obtained by evaluating the flux at $R = R_s$ as follows,

$$P^R_{v_0 j_0 k_0, i}(E) = \frac{\hbar}{\mu_R} \mathrm{Im}\left(\sum_{vjknn'} F^*_{nvjk,i}(E) u^*_n(R) \times \frac{\partial}{\partial R} u_{n'}(R) F_{n'vjk,i}(E) \right)_{R=R_s} \tag{3.3.3}$$

The cross section for electronic state i can be calculated by summing over the probability for all possible partial waves (total angular momentum J) [19],

$$\begin{aligned} \sigma_{j_0 v_0, i}(E) &= \frac{\pi}{k^2_{j_0 v_0}} \sum_J (2J+1) P^J_{j_0 v_0, i}(E) \\ P^J_{j_0 v_0, i}(E) &= \frac{1}{2j_0 + 1} \sum_{k_0} P^J_{j_0 k_0 v_0, i}(E) \end{aligned} \tag{3.3.4}$$

where $k_{j_0 v_0}$ is the initial wave number at a fixed collision energy.

4. Examples

4.1. *Nonadiabatic effects on the reaction mechanism of $F(^2P_{3/2}, ^2P_{1/2}) + H_2$ [97]*

We applied the improved time-dependent wave packet method to the benchmark $F + H_2$ reaction that is subjected to the previous elaborate time-independent scattering quantum calculations of Alexander *et al.* [31], and compared the calculated results of the two different quantum scattering methods. The Coriolis coupling is neglected in the present calculation (CS calculation).

The diabatic potential matrix (Alexander-Stark-Werner (ASW) potential energy surface [31]) and the spin–orbit coupling matrix used in the calculation are the same as those in the calculations of Alexander *et al.* [31], and can be expressed as:

	$\|0, 1/2\rangle$	$\|0, -1/2\rangle$	$\|1, 1/2\rangle$	$\|1, -1/2\rangle$	$\|-1, 1/2\rangle$	$\|-1, -1/2\rangle$
$\|0, 1/2\rangle$	V_Σ	0	$-V_1$	$-2^{1/2}$B	$-V_1$	0
$\|0, -1/2\rangle$	0	V_Σ	0	$-V_1$	$-2^{1/2}$B	$-V_1$
$\|1, 1/2\rangle$	$-V_1$	0	$V_\Pi - $A	0	V_2	0
$\|1, -1/2\rangle$	$-2^{1/2}$B	$-V_1$	0	$V_\Pi + $A	0	V_2
$\|-1, 1/2\rangle$	$-V_1$	$-2^{1/2}$B	V_2	0	$V_\Pi + $A	0
$\|-1, -1/2\rangle$	0	$-V_1$	0	V_2	0	$V_\Pi - $A

V_1, V_2, V_Σ, V_Π are the four terms of the diabatic potential energy surface, A and B are spin–orbit coupling terms. The six $|\lambda\sigma\rangle (\lambda = 0, \pm 1, \sigma = \pm 1/2)$ constitute the diabatic electronic basis. In preparing the initial wave packet, the transformation from the coupled electronic basis function to the uncoupled electronic basis function has been conducted and the two electronic bases are related to each other via the CG coefficients.

The diabatic coupling effects, i.e. the electronic coupling V_1 and V_2 on the reaction mechanism can be investigated by a comparison between the six-surface and the two-surface scattering calculations, with the latter one neglecting these two electronic coupling terms. In figures 1 and 2, we show the total reaction cross sections for the ground spin state $F(^2P_{3/2})$ and the excited spin state $F(^2P_{1/2})$ atoms (with H_2 in its ground initial rovibrational state), respectively. The results calculated on both six surfaces and on two surfaces are included. The corresponding time-independent

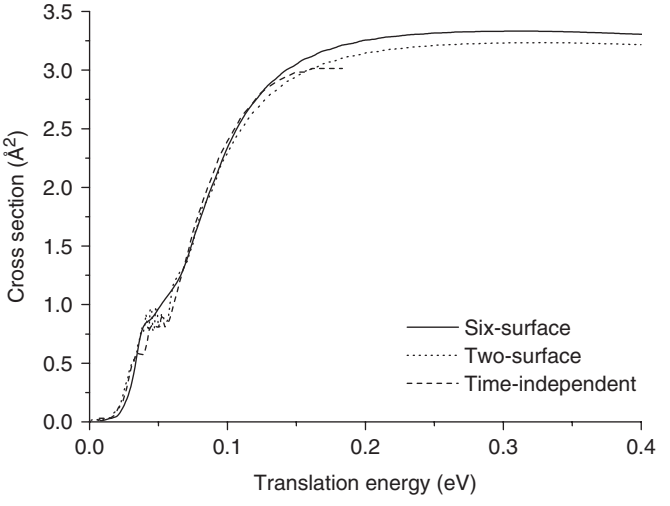

Figure 1. The total reaction cross sections on the two-surface and six-surface for the reaction of $F(^2P_{3/2})$ with H_2 ($v=j=0$) as a function of the translation energy [97]. The dashed lines correspond to the time-independent results reported by Alexander *et al.* [31].

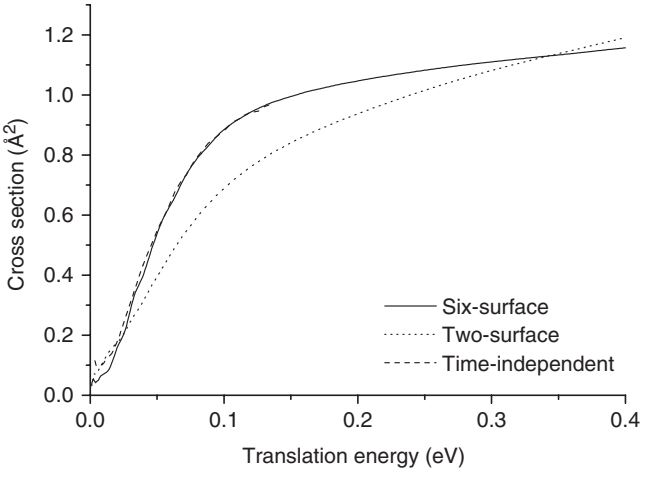

Figure 2. The total reaction cross sections on the two-surface and six-surface for the reaction of $F(^2P_{1/2})$ with H_2 ($v=j=0$) as a function of the translation energy [97]. The dashed lines correspond to the time-independent results reported by Alexander *et al.* [31].

quantum results of Alexander *et al.* [31] are also shown for comparison. For the excited $F(^2P_{1/2})$ atom, the agreement between the two different quantum calculations is nearly perfect, indicating that the Coriolis coupling slightly influences the reactivity of the excited F atom. However, in the case of the ground state $F(^2P_{3/2})$ atom, the present quantum results are larger than the time-independent cross sections at high collision energy, due to which the present quantum calculations neglect the Coriolis coupling. Further, we can see that, the excited $F(^2P_{1/2})$ atom has a larger internal energy and thus illustrates a higher reactivity than the ground $F(^2P_{3/2})$ atom with lower collision energy. Finally, the comparison between the two-surface and the six-surface calculated results has revealed that the electronic coupling terms do have effects on the reaction mechanism, and they affect the reactivity of the excited $F(^2P_{1/2})$ atom more than that of the ground $F(^2P_{3/2})$ atom.

4.2. *The reactivity of the ground and the excited spin state $F(^2P_{3/2},^2P_{1/2})$ atoms with D_2 [98]*

Here, the time-dependent wave packet method has been employed to investigate the role of the excited state in this reaction and compared with the previous study on the $F(^2P_{3/2},^2P_{1/2}) + H_2(v=0,\ j=0)$ reaction. We calculate the total reaction probability and the cross sections for the ground and the excited spin state F atoms, and further calculate the rate constant from the total cross sections $\sigma(E)$ as follows:

$$K(T) = \sqrt{\frac{8K_BT}{\pi\mu_R}}(K_BT)^{-2}\int_0^\infty E\sigma(E)\exp\left(-\frac{E}{K_BT}\right)dE \tag{4.2.1}$$

with K_B being the Boltzmann constant and E the collision energy.

Figure 3 shows the calculated total reaction cross sections on the ASW potential energy surface [31] for the ground and the excited state F atoms. For comparison, the single-surface results calculated on the lowest adiabatic ASW surface are also included in figure 3. At lower collision energies, the multiple surface result of the ground state F atom agrees well with the single-surface result, however, the former deviates down from the latter at higher collision energies, indicating an increasing role of the nonadiabatic effects with higher collision energies. Similar to $F + H_2$, the cross sections of the excited F atom are slightly larger than those of the ground state F atom at very low collision energies (see figure 4), but the cross sections of the ground and the excited states in this isotopic reaction are smaller than those in the $F + H_2$ reaction. The present quantum calculations also predict a rather lower reaction threshold of $\sim$0.1 kcal mol^{-1} as compared with the previous calculated values, i.e. $\sim$0.36 kcal mol^{-1} of Quantum Mechanical (QM) results on the Hartke-Stark Werner (HSW) potential energy surface [44], $\sim$0.92 kcal mol^{-1} of Quasi-Classical Trajectory (QCT) value on the Stark-Werner (SW) potential energy surface [80]. Figure 5 shows the calculated rate constant for the ground and the excited F atoms, along with the average rate constant. In this figure, the ground state rate constant is in good agreement with the average rate constant, suggesting that the excited state contributes little to the average rate constant. Indeed, it is found that the excited state contributes 0.9 and 3.1% to the overall reactivity at 200 (corresponding to 5(1000/200) in figure 5) and 500 K (corresponding to 5(1000/500) in figure 5), respectively.

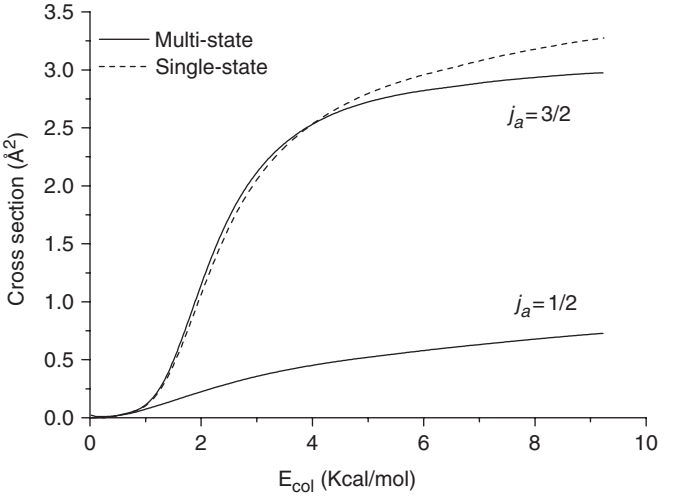

Figure 3. Total multi-state cross sections for the $F(^2P_{3/2,1/2}) + D_2$ ($v = j = 0$) reaction, as a function of the collision energy (solid line) and the single-state cross section (dashed line), taken from [98].

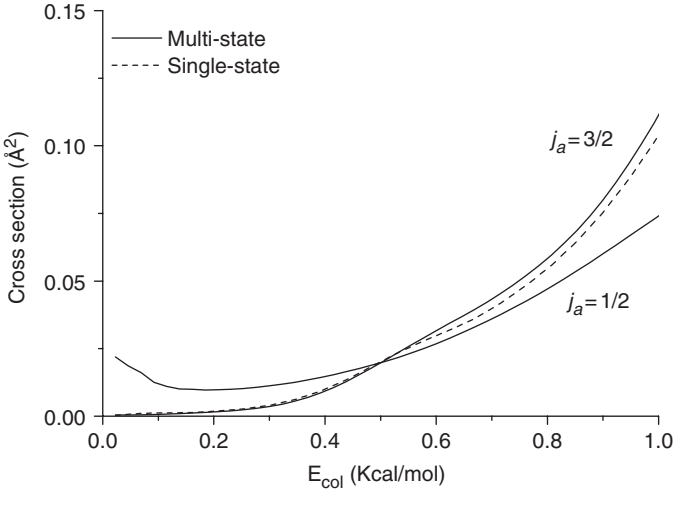

Figure 4. Total multi-state cross sections for the $F(^2P_{3/2,1/2}) + D_2$ ($v = 0$, $j = 0$) reaction at very low collision energy (solid line) and the single-state cross section (dashed line), taken from [98].

4.3. *Nonadiabatic investigation on the $F(^2P_{3/2},^2P_{1/2}) + HD$ reaction [99, 100]*

The two product channels FH + D and FD + H in this reaction were investigated by calculating their reaction probabilities and the total reaction cross sections deriving from the initial rovibrational state $v = 0$, $j = 0, 1$ of the reactant HD, and the present time-dependent wave packet quantum results are compared with the existing experimental measurement and the single-surface calculated results [81].

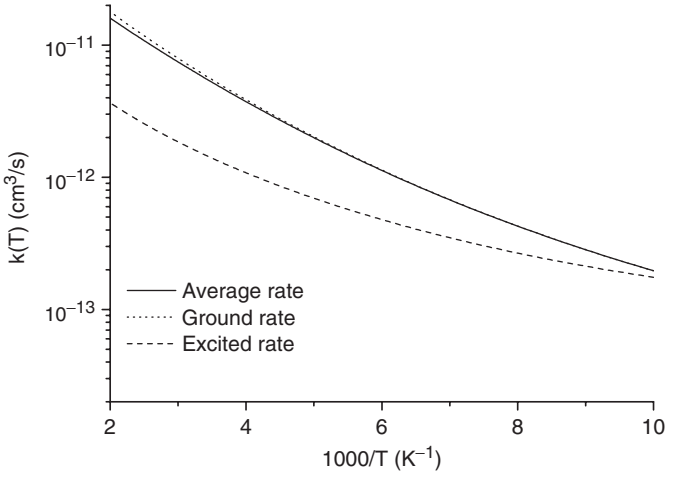

Figure 5. Average $v=0$, $j=0$ rate constant, along with the ground and the excited state rate constants for the reaction of $F(^2P_{3/2},^2P_{1/2}) + D_2$ [98].

The total reaction cross sections calculated on the ASW potential energy surface [31] for $j=0$ and $j=1$ are shown in figure 6. Similar to the $F + H_2$ reaction, at lower collision energies, the cross sections of the excited state are slightly larger than those of the ground state, and such behaviour is more obvious in the DF + H channel than in the HF + D channel. As far as the DF + H channel is concerned, such behaviour is much more obvious with $j=1$ than $j=0$. Furthermore, the $j=0$ cross sections of the ground state show a clear resonance peak in low collision energy region for the HF + D channel.

In figure 7, we compare the experimental measurement [81] with the averaged cross sections, calculated from the reaction cross sections, with 80% of HD in $j=0$ state, 20% in $j=1$ state and 16% of F in excited spin state as well. It can be seen that the calculated resonance peak appears at the collision energy about 0.4 kcal mol^{-1} higher than the experimental one, and this is probably due to the spin–orbit coupling which causes an increase of 0.375 kcal mol^{-1} in the barrier height on the ASW surface [31]. The height of the peak is about 1.3 times that of the experimental result [81]. When compared with the single-surface calculated cross sections on the SW surface [81], which is about 2 times that of the experimental result, the present calculation has lowered the height of the resonance peak, thus suggesting a relatively important role of the spin–orbit coupling in the reaction mechanism.

We further modify the ASW surface by lowering its barrier height using the scale external correlation technique, and perform again the quantum dynamics calculation on this modified ASW (MASW) surface to obtain the total reaction cross sections for $F + HD(v=0, j=0)$ and $F + HD(v=0, j=1)$. We note here that the barrier height on the ASW surface is lowered by 0.015 and 0.016 eV for the collinear and the lowest bent configuration barriers, respectively after the modification. The cross sections for two initial states $j=0$ and $j=1$ of the HD-molecule, calculated on the MASW surface, are shown in figures 8 and 9, and the averaged cross sections are compared with the

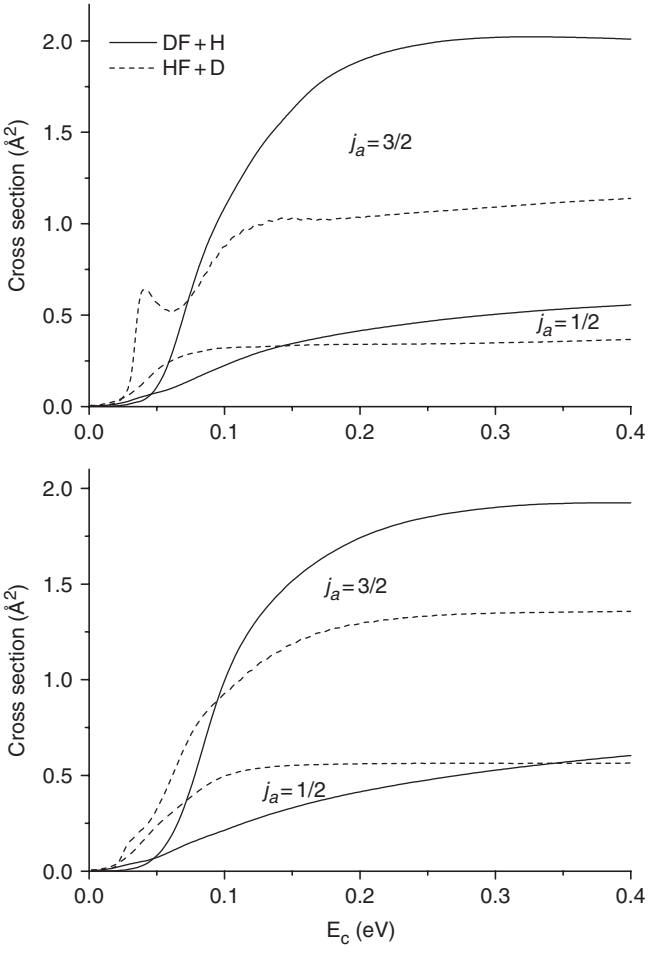

Figure 6. The total integral cross sections for the reaction of F($^2P_{3/2}$,$^2P_{1/2}$) with HD in $j=0$ (upper panel) and 1 (lower panel) as a function of the collision energy, taken from [99].

experimental results [81] and with our calculated results on the ASW surface in figure 10, the single-surface results on the SW surface of Skodje *et al.* [81] are also shown for comparison. It is clear that the quantum wave packet calculation employing the MASW surface also reproduced the experimentally observed resonance feature in the total reaction cross sections of the HF + D channel (see figure 8). Compared with the above ASW-surface results, this time the resonance peak appeared at a rather lower collision energy of 0.026 eV, getting close to the experimental observations. The good agreement of the peak position and yet the reduced peak height from 2.96 a_0^2 on the SW surface to the 2.06 a_0^2 on the present MASW surface, as revealed by the comparison between the single-surface and the MASW-surface results, indicates that the MASW surface has almost the same adiabatic barrier as the adiabatic SW surface, as well as that the spin–orbit coupling has a substantial effect on the resonance feature. For the

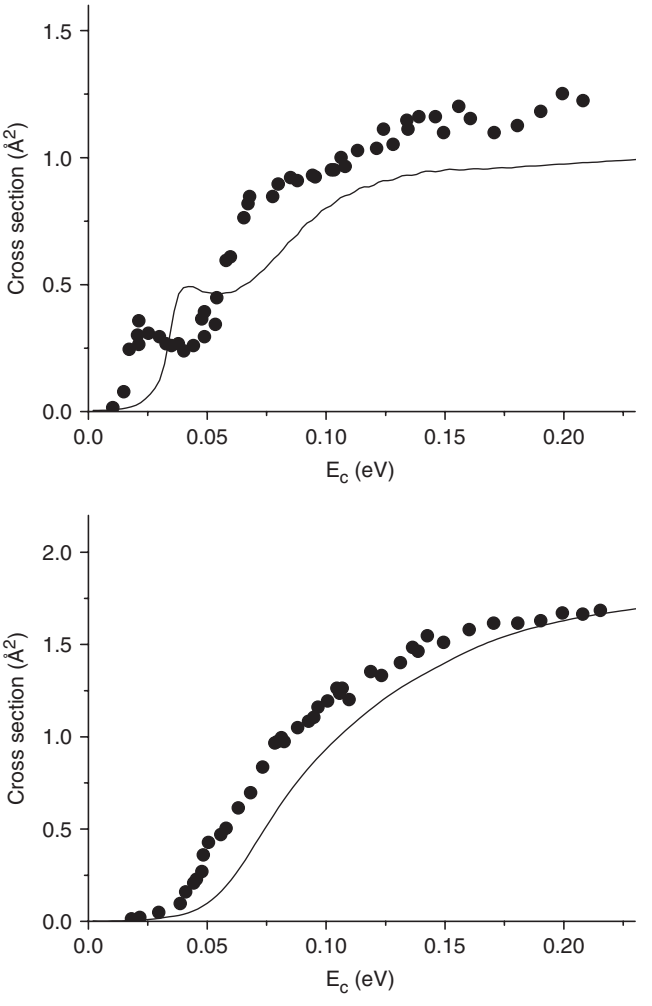

Figure 7. Comparison of the averaged cross section for the reaction with 80% HD($j=0$) and 20% HD($j=1$) with the experimental results from [81]. The upper and the lower panels correspond to the reaction of $F+HD \rightarrow HF+D$ and $F+HD \rightarrow DF+H$, taken from [99].

$DF+H$ channel, the lowered barrier on the MASW surface causes an energy shift of 0.015 eV to lower energy region in the MASW results as compared with the ASW results, and thus achieves a nearly perfect agreement with the experimental measurements.

The isotopic effect $\sigma_{DF+H}/\sigma_{HF+D}$ of this reaction can be seen by the branching ratio of the ground and the excited states with HD in $j=0$ and $j=1$. Here, the results are derived from the calculated cross sections on the ASW surface. As shown in figure 11, the difference between the isotopic effects of the ground and the excited states lies in that at lower collision energies, the isotopic effect of the excited state is much more stronger than that at the ground state, because the initial internal energy and the

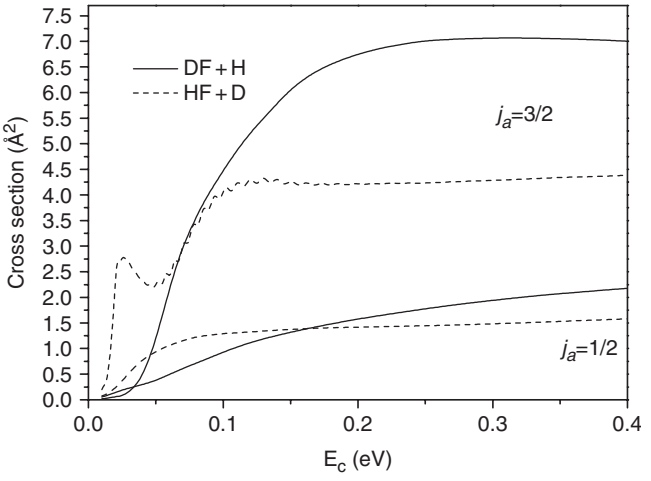

Figure 8. The total integral cross sections for the reaction of F($^2P_{3/2}$,$^2P_{1/2}$) with HD in $v=0$, $j=0$ as a function of the collision energy on the MASW surface [100].

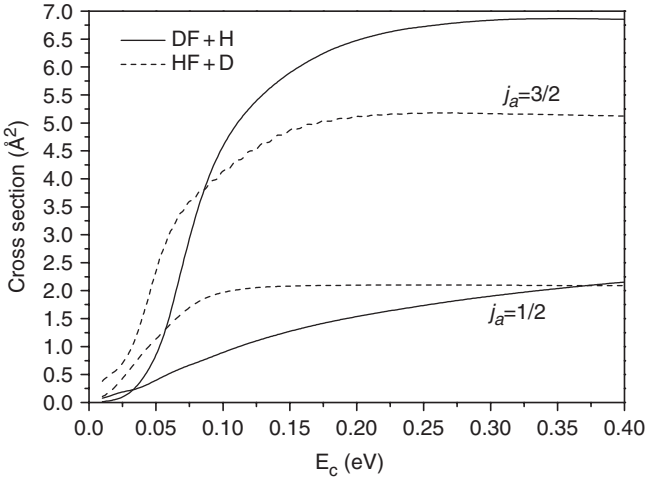

Figure 9. The total integral cross sections for the reaction of F($^2P_{3/2}$,$^2P_{1/2}$) with HD in $v=0$, $j=1$ as a function of the collision energy on the MASW surface, taken from [100].

electronic angular momenta are different for the excited and the ground states. Finally, we show the energy-dependent reactivity of the excited state $I=\sigma(P_{1/2})/\sigma(P_{3/2})$ for the two product channels with HD in $j=0$ and $j=1$ in figure 12. At low collision energies, the reactivity of the excited state is larger than 1, and the largest value with $j=1$ is found to be $\sim$0.012 and 0.018 eV for the HF + D and DF + H channels, respectively. As the collision energy increases, the reactivity of the excited state gradually decreases, and is no more than 43% of reactivity of the ground state at a higher collision energy.

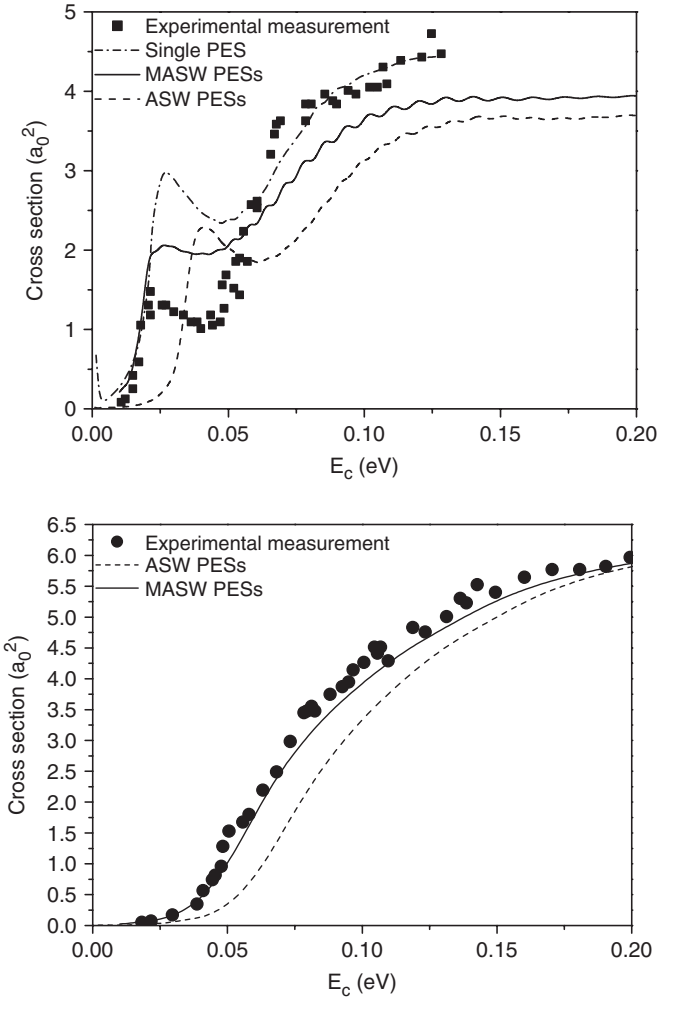

Figure 10. Comparison of the averaged cross section for the reaction with 80% HD($v=0$, $j=0$) and 20% HD($v=0$, $j=1$) with the experimental results [81] and other theoretical calculation (ASW PESs calculation from [99], single PES result form [81]). The upper and lower panels correspond to the reaction of $F + HD \rightarrow HF + D$ and $F + HD \rightarrow DF + H$, taken from [100].

4.4. *Electronic quenching process in the $O(^1D) + N_2 \rightarrow O(^3P) + N_2$ reaction [101]*

The issue is of great theoretical interest due to its importance in atmospheric chemistry. Both the heavy reactant and the deep potential well on the ground singlet potential surface present the challenge to the quantum study, and the only previous time-independent quantum calculation was that of Takayanagi [70], in which a two-surface collision model is used to describe the electronic quenching process. In our time-dependent study, both the three-surface and two-surface collision models are used to investigate the role of the second excited state in the quenching process. One advantage of the time-dependent wave packet method over the time-independent quantum method

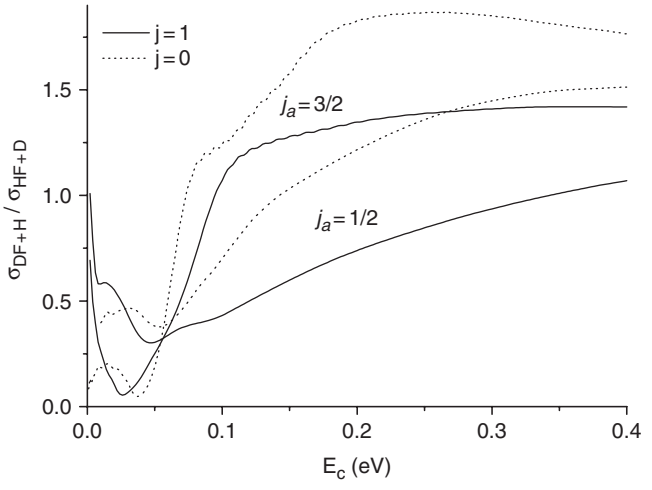

Figure 11. The branching ratio for the reaction of $F(^2P_{3/2}, ^2P_{1/2})$ with HD in $j=0$ and $j=1$ as a function of the collision energy, taken from [99].

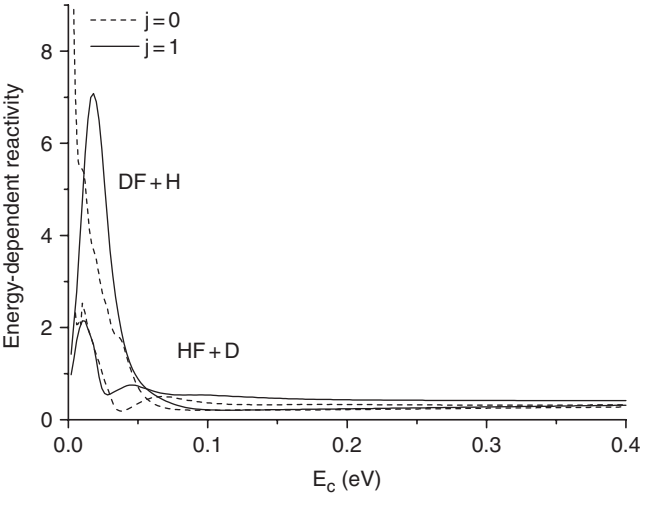

Figure 12. The energy-dependent reactivity of the spin–orbit excited state for the reaction of $F(^2P_{3/2}, ^2P_{1/2})$ with HD in $j=0$ and $j=1$ as a function of the collision energy, taken from [99].

is that the information over a range of collision energies can be determined in a single calculation which help in investigating if the resonance feature exists in the calculated total electronic quenching cross sections, and enables to find the information that lacks in the time-independent quantum calculation. The present time-dependent results are also compared with the experimental data [82] and the previous theoretical results [70, 71].

The adiabatic potential energy surfaces of the $^1A'$, $^3A'$, and $^3A''$ states and the spin–orbit couplings between the singlet and triplet states are used in the quantum calculations. Three different types of singlet surface, the model surface ZPM2 of Miller *et al*. [71], and the *ab initio* fitted DMBE2 surface of Nakamura and Kato [83] as well as the modified DMBE2 surface by the author, along with the constant spin–orbit coupling of 80 cm^{-1}, and the analytical spin–orbit coupling of Nakamura and Kato [83] are employed to study the influence of the singlet potential surface and the spin–orbit coupling on the reaction mechanism. The triplet surfaces used here are those fitted to *ab initio* calculated energy points by Nakamura and Kato [83]. The CS approximation is employed in the calculation for total angular momentum $J>0$, and the electronic angular momenta are neglected in the Hamiltonian of the system.

Figure 13 shows the time evolution of the calculated probabilities within the two-surface collision model including the DMBE2 singlet surface for the total angular momentum $J=10$. It is clear that a propagation time of 350000 a.u. is sufficient for obtaining the converged results. For each J, the calculation within the three-surface collision model costs about 250 h of CPU time using Xeon 2.1 GHz processor, indicating the difficulty for performing quantum calculations for this reaction system.

Figures 14 and 15 present the total quenching cross sections calculated on the original/modified DMBE2 surface and on the ZPM2 surface, using both analytical and constant spin–orbit couplings, and based on both two-surface and three-surface collision models. In our modified DMBE2 singlet surface, the faked barrier that caused the energy threshold behavior of the calculated probabilities has been removed without sacrificing its topological character. For the ZPM2 surface and the modified DMBE2 surface, we estimated the total quenching cross sections from the capture model of Gray *et al*. [53] to save the computational resources. Two experimentally measured cross sections [82] and the previous theoretical results [70, 71] are also shown for comparison. The calculated quenching cross sections on the DMBE2 surface within the two-surface model have shown no obvious resonance features, which is totally contrasting to the calculated reaction probability. Compared with the DMBE2 calculation, the energy threshold behavior of the quenching cross section on the modified DMBE2 surface also disappears, and the calculation on the modified DMBE2 surface produced larger cross sections. There is a reasonable agreement between the modified DMBE2 results within the three-surface collision model and the experimental measurement at 8 ± 6 kcal mol^{-1} (0.347 ± 0.26 eV), though the calculated results seem to be somewhat smaller than the experimental data at a collision energy of about 1 kcal mol^{-1} (0.04 eV). Further, the present ZPM2 cross sections are larger than the time-independent quantum results, but are smaller than the TSH result by Miller and coworkers [71]. It is found that the cross sections estimated on the ZPM2 surface with the analytical spin–orbit coupling within the three-surface collision model agree well with the experimental data measured at about 1 kcal mol^{-1}, and it seems that the ZPM2 results tend to agree with the experimental data at 8 ± 6 kcal mol^{-1}. Further, the insensitivity of the resonance structure in the calculated reaction probability to the spin–orbit function form, and the remarkable influence of the singlet surface on the calculated reaction probability, as well as the almost equal role of the second excited state $^3A''$ to the first excited state $^3A'$ in the electronic quenching process have been revealed in this study, with the first two further confirming the previous quantum time-independent study [70].

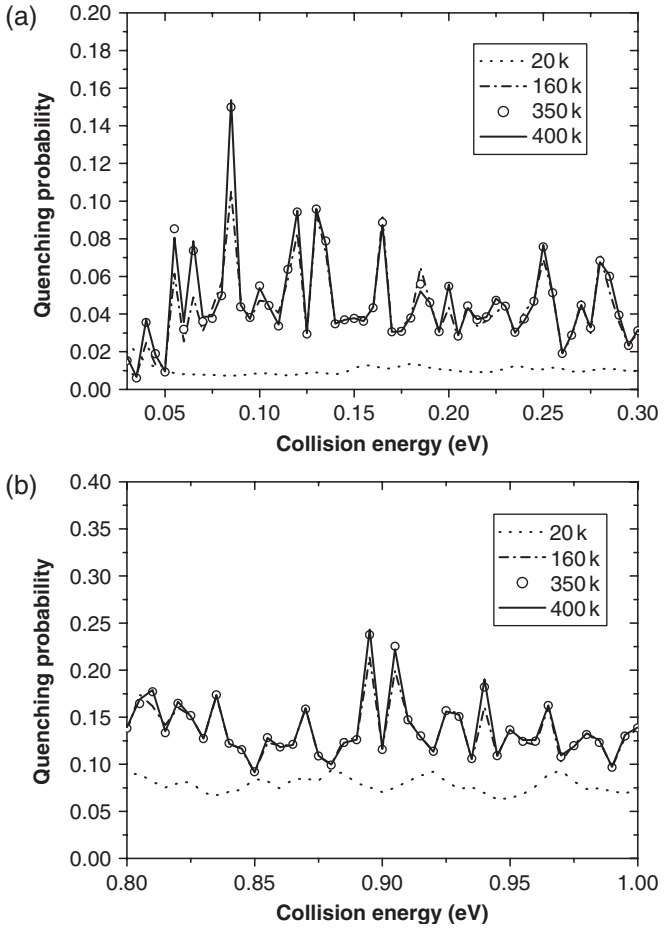

Figure 13. Probabilities obtained at different propagation time on two coupled surfaces, including the DMBE2 singlet surface for $J=10$. (a) The energy range here is $0.03 \sim 0.3$ eV. (b) The energy range is $0.8 \sim 1.0$ eV. Unit of time: a.u., taken from [101].

4.5. *The intersystem crossing effects in the $O(^3P,^1D) + H_2$ reaction [102]*

The difficulty for performing a quantum study partly arises from the fact that too many electronic states are involved in this issue and also that there is a deep potential well on the singlet potential energy surface. The only previous two TSH studies on the intersystem crossing effects were those of Schatz *et al.* [55, 56]. Here, we present our time-dependent quantum calculations on the issue and compare them with the corresponding TSH results.

The present calculations employed the four adiabatic potential energy surfaces of the $^3A''$, $^3A''$, $^3A'$ states of Kuppermann and co-workers [84] and $^1A'$ state of Dobby and Knowles [85], and the spin–orbit couplings of Schatz and Maiti [56]. In figures 16–19, we show the fine-structure resolved quantum cross sections for the wave packet initially on the four electronic states of $^3A''(1)$, $^3A''(2)$, $^3A'$, and $^1A'$ asymptotically correlating

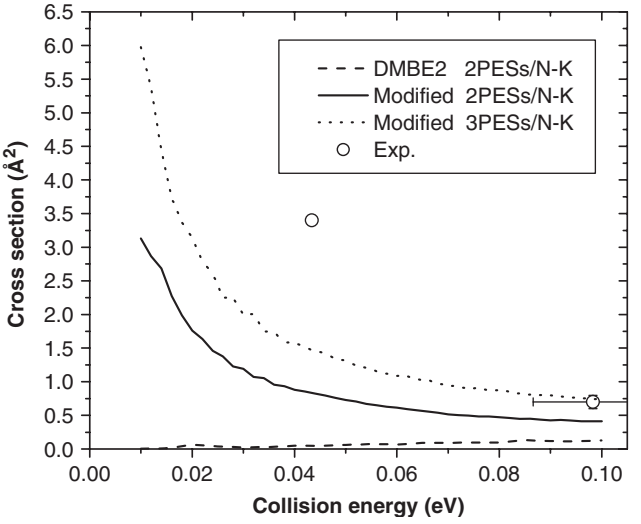

Figure 14. Cross sections on the original/modified DMBE2 surface in the collision energy range of 0.01∼0.1 eV. Dashed line – calculated on the original DMBE2 surface using two coupled surfaces and Nakamura–Kato spin–orbit coupling. Solid line – estimated on the modified DMBE2 surface using two coupled surfaces and Nakamura–Kato spin–orbit coupling (taken from [101]). Dotted line – estimated on the modified DMBE2 surface using three coupled surfaces and Nakamura–Kato spin–orbit couplings and taken from [101]. Open circles without and with the error bar are experimental data deduced by thermal rate constant and taken from [82], respectively.

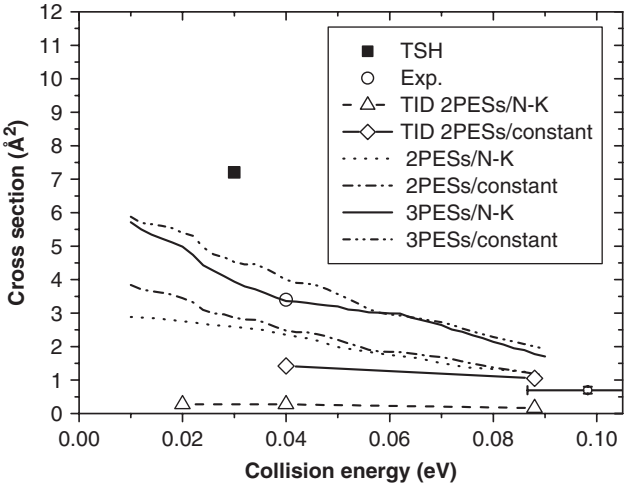

Figure 15. Cross sections on the ZPM2 surface estimated by the capture model at the collision energy range of 0.01∼0.1 eV (taken from [101]). Dotted line – two coupled surfaces with Nakamura–Kato spin–orbit couplings. Dash dotted line – two coupled surfaces with constant spin–orbit coupling of 80 cm^{-1}. Solid line – three coupled surfaces with Nakamura–Kato spin–orbit coupling. Dash dot dotted line – three coupled surfaces with constant spin–orbit coupling of 80 cm^{-1}. Solid square – trajectory surface hopping result taken from [71]. Open circles – experimental data taken from [84] and deduced from the thermal rate constant. Dashed line with open triangles and solid line with open diamonds correspond to the time-independent quantum results taken from [70].

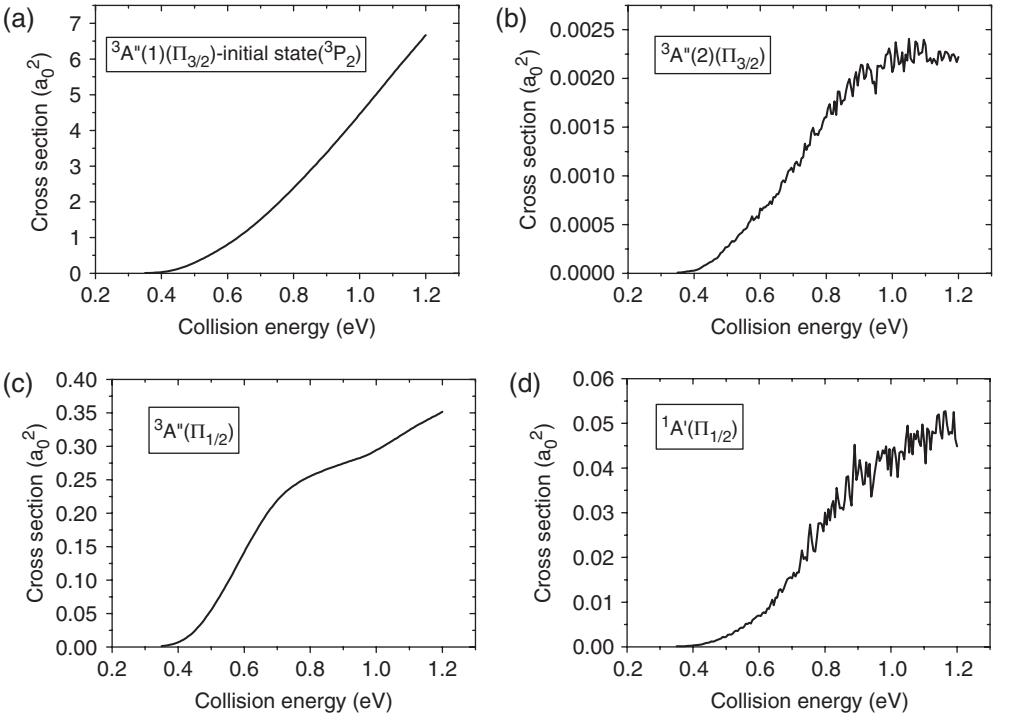

Figure 16. Calculated product fine structure resolved cross sections derived from ground rovibrational initial state as a function of collision energy of $0.35 \sim 1.2$ eV for the wave packet initially on the $^3A''(1)$ surface asymptotically correlating to the reactant fine structure $O(^3P_2) + H_2$. (a) Cross section obtained on initial propagated surface $^3A''(1)$. (b)–(d) The three cross sections caused by the spin–orbit-induced transition. Here they correlate to $^3A''(2)$, $^3A'$, and $^1A'$ surfaces, respectively (taken from [102]).

to the reactant fine-structure of $O(^3P_2,^3P_1,^3P_0,^1D_2) + H_2$. In the $O(^3P_2) + H_2$ reaction, it is found that the largest nonadiabatic transition is to the $^3A'$ ($\Pi_{1/2}$) state, with a branch ratio of $5 \sim 20\%$. The next is to the $^1A'$ ($\Pi_{1/2}$) state, with a branch ratio of $0.6 \sim 1.8\%$, and the smallest is to the $^3A''(2)$ ($\Pi_{3/2}$) state, with a branch ratio of $0.03 \sim 0.1\%$. In the case of $O(^3P_1) + H_2$, the nonadiabatic transition to the $^1A'$, $^3A'$, and $^3A''(1)$ states has a branch ratio of $1.5 \sim 4.8\%$, $1 \sim 2.6\%$, and $0.07 \sim 0.58\%$, respectively. With respect to the fine structure $O(^3P_0) + H_2$, the largest spin–orbit-induced nonadiabatic transition is to the $^3A''(1)$ state, with a branch ratio of $11.6 \sim 56.6\%$, followed by the transition to the $^3A''(2)$ state with a branch ratio of $0.45 \sim 1.7\%$, and the least is the transition to the $^1A'$ state with a branch ratio of $0.1 \sim 1.1\%$. The rather large branch ratio of the transition to the $^3A''(1)$ state, for example, 50% at 0.465 eV and 40% at 0.54 eV, indicates that at some collision energies the spin–orbit coupling between $^3A'$ and $^3A''(1)$ has significant contribution to the intersystem crossing in the $O(^3P_0) + H_2$ reaction. As for the $O(^1D_2) + H_2$ reactant fine structure, the transition to the $^3A''(1)$, $^3A''(2)$, and $^3A'$ state has a branch ratio of $0.27 \sim 0.33\%$, $1.17 \sim 1.66\%$, $0.16 \sim 0.22\%$, respectively. It should be noted that the investigated collision energy range for the triplet state is different from that of the singlet state. Furthermore, the unique quantum resonance

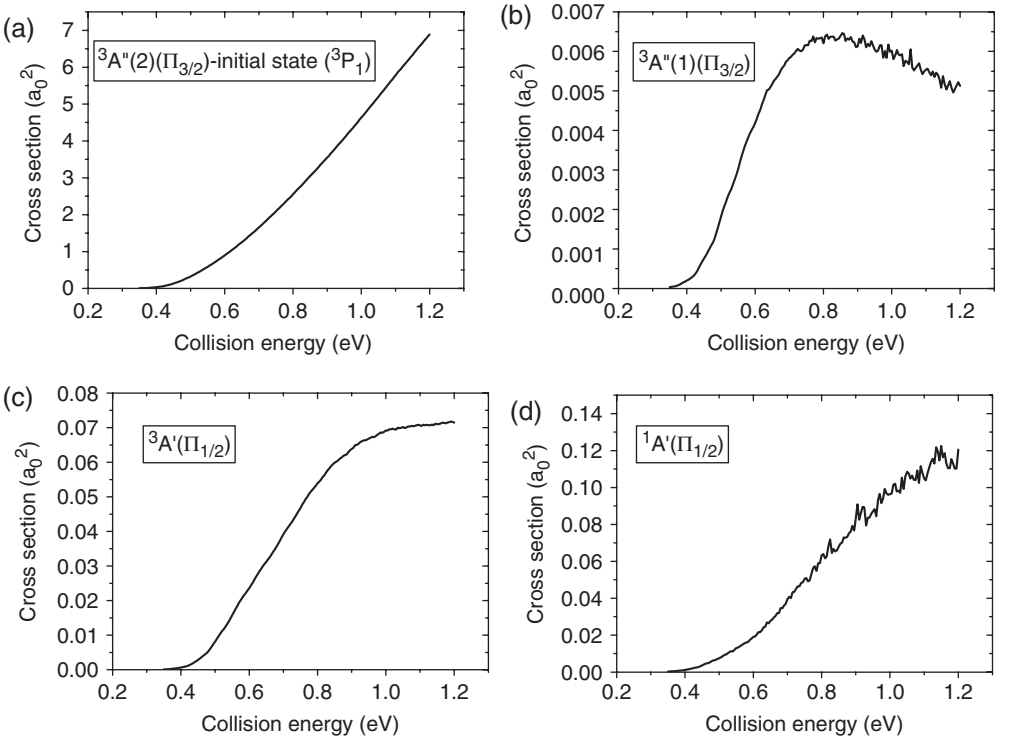

Figure 17. The same as figure 20, but for the wave packet initially on the $^3A''(2)$ surface asymptotically correlating to the reactant fine structure $O(^3P_1) + H_2$. (a) On the $^3A''(2)$ surface, (b) on the $^3A''(1)$ surface, (c) on the $^3A'$ surface, and (d) on the $^1A'$ surface. (taken from [102].)

features are also observed in some of the calculated cross sections. The quantum dynamics calculations showed that the transitions between the triplet states of different symmetries, especially those between $^3A'$ and $^3A''(1)$, play more significant roles than the transitions between the singlet and triplet states during the intersystem crossing. Such transitions are particularly efficient at certain low collision energies in the case of the reactant fine structure $O(^3P_0) + H_2$. The roles of the singlet–triplet transitions are negligible for branch ratios below 5%. However, the effects of the spin–orbit coupling on the total reaction cross sections, obtained by averaging the fine-structure resolved cross sections in the $O(^3P_{2,1,0}) + H_2$ reaction, are insignificant. This agrees with the recent studies of Braunstein *et al.* [86] and Balakrishnan [87].

Figure 20 shows the product ratio of the OH spin state $\Pi_{3/2}$ to $\Pi_{1/2}$ for the wave packet initially on the triplet surfaces. The value stays at around 2.75 : 1 at collision energies higher than 0.6 eV, while it covers a wide range of $3:1 \sim 5:1$ at lower energies. The present ratio is a little higher in comparison with the TSH ratio of approximate 2 : 1. As shown in figure 21, the comparison between the previously reported [56] and the present quantum results shows a qualitative agreement, but some differences are also found in the comparison. The present study yields a lower threshold than the TSH study for the barrier processes due to the tunneling effects. At high energies,

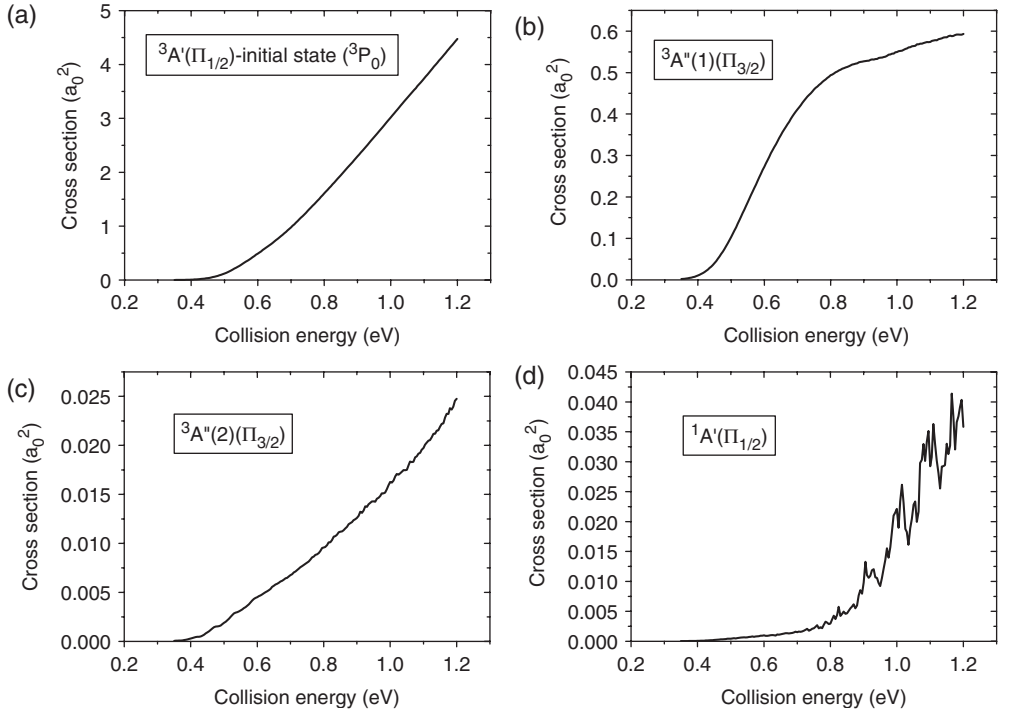

Figure 18. The same as figure 20, but for the initial wave packet on the $^3A'$ surface asymptotically correlating to the reactant fine structure $O(^3P_0)+H_2$. (a) On the $^3A'$ surface. (b) On the $^3A''(1)$ surface. (c) On the $^3A''(2)$ surface. (d) On the $^1A'$ surface. Taken from [102].

the product fine-structure resolved cross sections by the present quantum calculation are smaller than the TSH cross sections for the $O(^3P_{2,1,0})+H_2$ reaction, and the only exception is the $\Pi_{3/2}$ cross section in the $O(^3P_0)+H_2$ case, where the quantum result is larger than the TSH result. This suggests that the present quantum calculation has revealed a more significant role of the coupling between the triplet states of different symmetries than the TSH calculation. For $O(^1D_2)+H_2$ case, the present calculation yielded a larger cross section for the product spin state $\Pi_{1/2}$ and a smaller one for the product spin state $\Pi_{3/2}$.

4.6. *Nonadiabatic quantum calculations on the $D^+ + H_2$ reaction [103]*

The impetus behind our theoretical investigation in this reaction system is to make a direct comparison between the theoretically calculated quantities and the experimental measurements, since almost all the previous time-independent quantum calculations are limited to the total angular momentum $J=0$. The deep singlet potential well still challenges the quantum calculations though this light system lending itself easily to the exact quantum dynamical calculations.

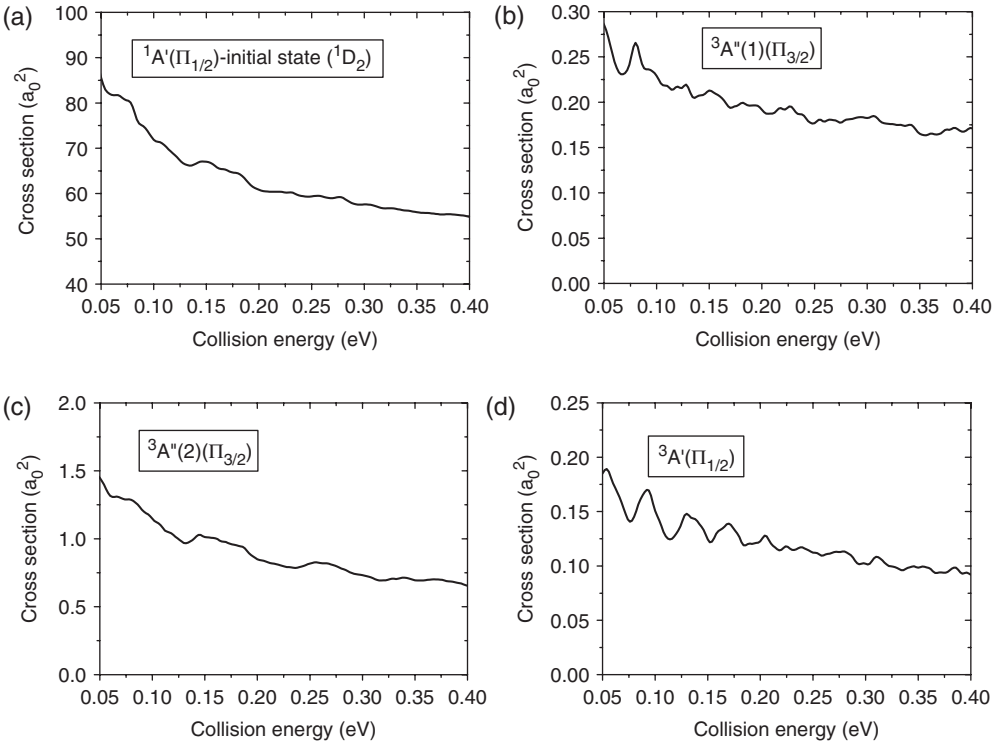

Figure 19. The same as figure 20, but for the initial wave packet on the ^{1}A′ surface asymptotically correlating to the reactant fine structure $O(^1D_2) + H_2$ within collision energy range $0.05 \sim 0.4$ eV. (a) On the ^{1}A′ surface. (b) On the ^{3}A″(1) surface. (c) On the ^{3}A″(2) surface. (d) On the ^{3}A′ surface. Taken from [102].

We studied the three competitive channels of the reactive charge transfer (RCT), the nonreactive charge transfer (NRCT), and the reactive no charge transfer (RNCT) in this reaction system. Three electronic states of 1^1A′, 2^1A′, and 3^1A′ are involved in the nonadiabatic processes and the corresponding diabatic Kamisaka-Bian-Nobusada-Nakamura (KBNN) potential matrix, recently fitted to *ab initio* data by Nakamura and co-workers [64], are employed in the quantum calculations. The present time-dependent quantum probabilities for $J = 0$ are compared with the time-independent quantum results [64], and the calculated total reaction cross section are compared with the experimental measurements [88]. We carried out the coupled-channel (CC) calculations and the number of K used in the CC calculations is up to 5.

A comparison of the present calculated probabilities for $J = 0$ of the RCT and NRCT channels with the time-independent results [64] in figure 22, shows a reasonable agreement between the two results with rich resonance structure and similar energy threshold. But the peak positions and the peak widths of the resonances are different, probably arising from the different dynamical scheme, and such differences have little effect on the calculated cross sections since many of these resonance structures would be washed out through J-sum. As we already mentioned above, both the time-dependent and time-independent quantum scattering calculations produced the same results for

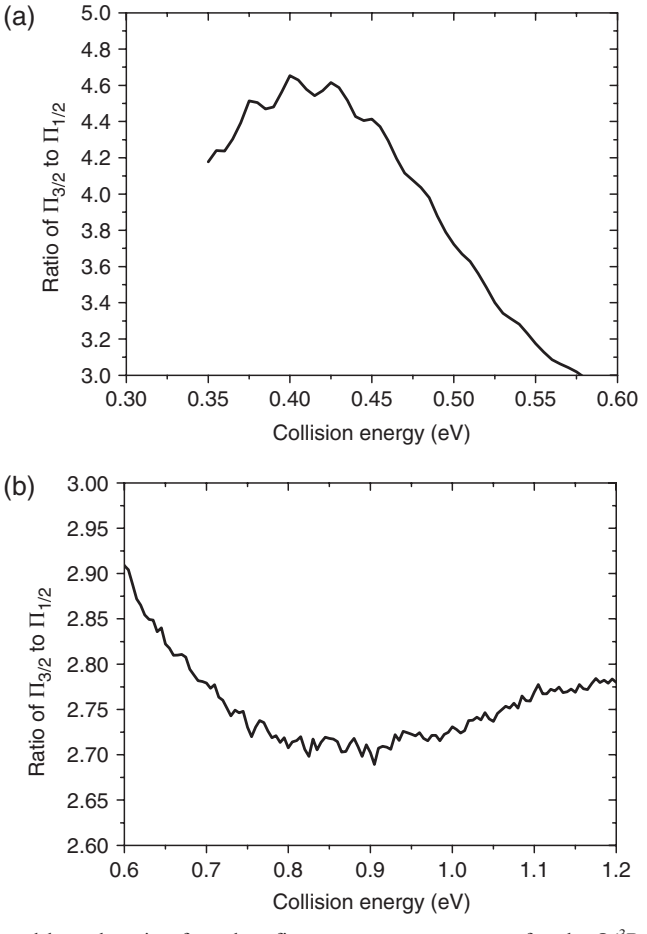

Figure 20. Calculated branch ratio of product fine structure $\Pi_{3/2}$ to $\Pi_{1/2}$ for the $O(^3P_{2,1,0}) + H_2$ reaction. (a) For low collision energy. (b) For high collision energy. (taken from [102].)

the abstraction reaction of $F + H_2$. Also, it seems to be hard to get the converged results for the $D^+ + H_2$ reaction by using the time-independent approach since no time-independent quantum cross sections have been reported thus far. Therefore, the difference we show here may suggest that the time-dependent wave packet method is probably more suitable for describing the reactions in which the long-lived complex is formed than the time-independent quantum method.

Because the experimental data for NRCT is still lacking thus far, we showed the present quantum cross sections deriving from the initial rovibrational state $v = 0$, $j = 0$ of reactant H_2 for the RNCT and RCT channels, along with the existing experimental measured cross sections [88] in figure 23. The present quantum calculations give a threshold of about 1.8 eV for the RCT channel, which is in good agreement with the experimental value of 1.82 eV. Also, the RCT cross sections agree reasonably well with the experimental results. The computed quantum values for the RNCT channel

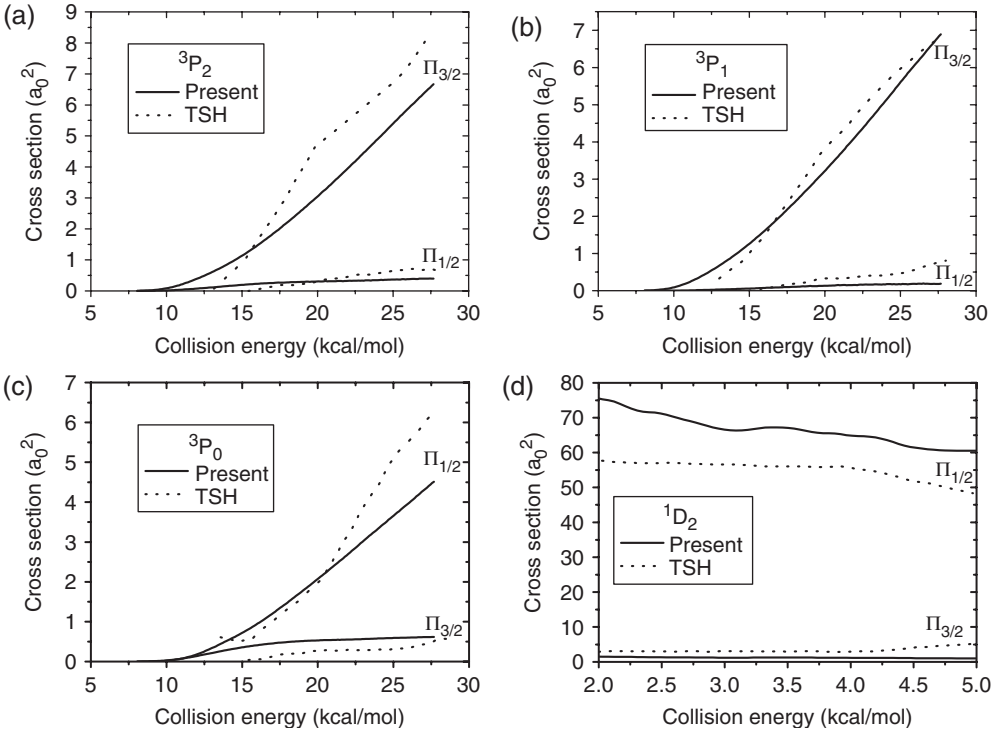

Figure 21. Comparison of the cross sections of product OH spin state $\Pi_{3/2}$ and $\Pi_{1/2}$ between the previous TSH study and the present quantum scattering calculation. Dotted line – TSH results taken from [56]. Solid line – quantum results taken from [102].

are somewhat higher than the experimental results. One of the most probable reasons for the discrepancy between the RNCT values and the experimental results is that the present calculations were carried out for the ground rovibrational initial state of the reactant H_2, whereas the experimental data were measured at room temperature. Therefore, a more reasonable comparison should be made between the $j=1$ calculation and the experimental data.

The present quantum calculations illustrated that the RNCT is the dominant channel in the reaction of $D^+ + H_2(v=0, j=0)$, and thus leads to a dominant insertion reaction mechanism. But the nonadiabatic channels of RCT and NRCT will gradually open up for a higher collision energy. The alternative ascending fashion of the RCT and NRCT cross sections, as shown in Figure 24, indicates that the two nonadiabatic channels are very competitive and comparable to each other at lower collision energies, but once the collision energy exceeds 2.2 eV, the cross section of the RCT rises rapidly and becomes the favoured channel. In addition, the strong v-dependence of the calculated probabilities has also been revealed in the present quantum calculations, and thus predicted that the vibrational excitation of the reactant H_2, especially its closest level to the surface crossing of $v=4$, plays a very important role in the electronically nonadiabatic transitions of the reaction system.

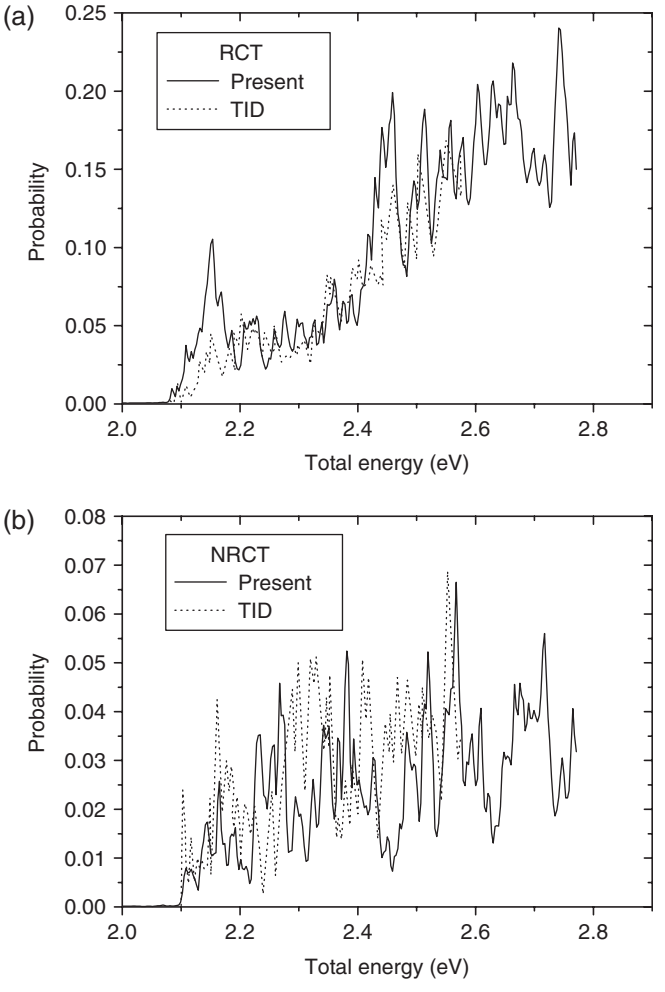

Figure 22. A comparison of probabilities for $J=0$ between the previous time-independent [64] and the present time-dependent quantum studies. (a) RCT. (b) NRCT, taken from [103].

4.7. *Nonadiabatic investigation on the $H^+ + D_2$ reaction [104]*

Compared with the $D^+ + H_2$ reaction, this isotopic variant is heavier and less studied by theorists. Similar to $D^+ + H_2$, we calculated the total reaction probabilities and the total reaction cross sections for the RCT, NRCT, and RNCT channels by performing the CC calculations on the KBNN diabatic potential energy surface [64]. The quantum cross sections are compared with experimental measurements [89] and with TSH results [69]. We also discussed the underlying mechanism for the reaction system.

The total reaction cross sections deriving from the initial ground rovibrational state of D_2 of the three channels are shown in figure 25, along with the experimental measurements [89] and the previous TSH results [69]. There is an overall agreement between the experimental and the present quantum results, with better agreement at

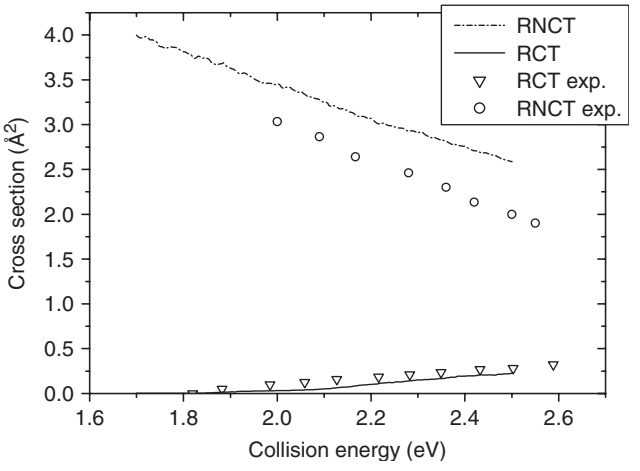

Figure 23. A comparison between the experimental data [88] and the present calculated quantum cross sections; taken from [103].

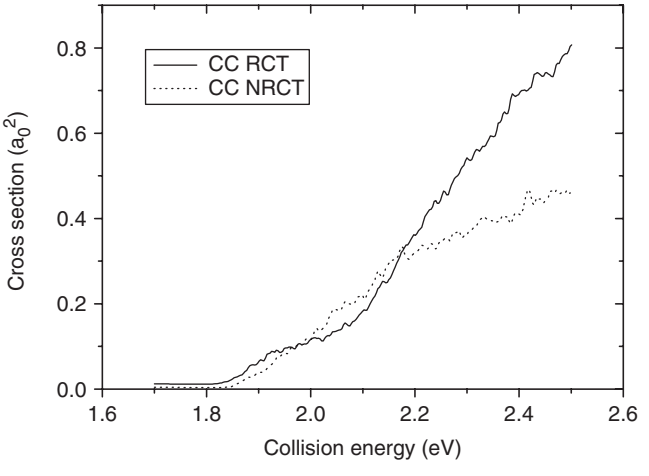

Figure 24. Computed cross sections for the two nonadiabatic processes of the RCT and NRCT (from [103]).

higher collision energies than at lower collision energies. For RCT, the present quantum calculations give a threshold of about 1.90 eV, which is in better agreement with the experimental value of 1.86 eV than the TSH calculated value of 2.01 eV. Compared with the TSH results, the present quantum calculations produce much larger cross sections. Of the two nonadiabatic channels, the NRCT channel is found to be slightly preferential over the RCT channel in this isotopic reaction (see figure 26), different from the $D^+ + H_2$ reaction system. The reason probably lies in the fact that the heavy isotopic mass of the reaction system makes it rather difficult for the reactant to surmount the barrier on the excited surfaces to form the RCT channel.

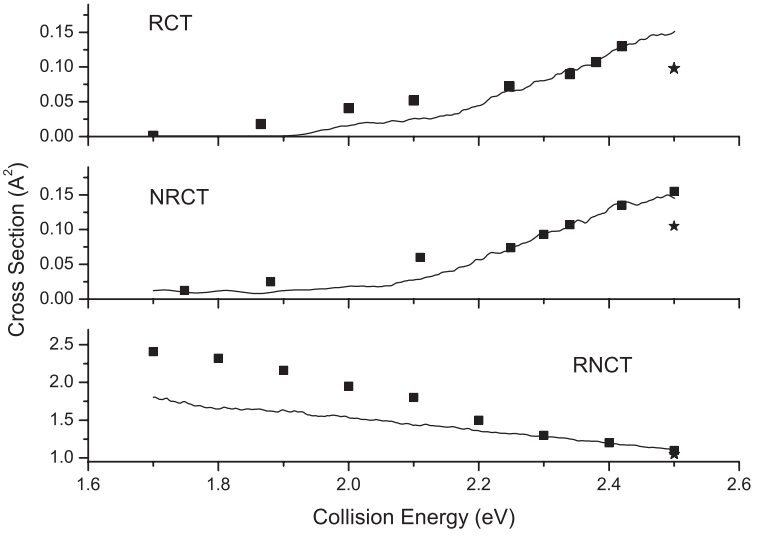

Figure 25. Comparison among the present quantum cross sections, experiment measurements of Teloy *et al.* [89] and TSH calculation of Yokoyama *et al.* [69]. Solid line, closed square and star correspond to the present work, the experimental data and the TSH results respectively; taken from [104].

Hence, similar to the $D^+ + H_2$ reaction, the largest RNCT cross sections indicate the dominant insertion reaction mechanism in the case of $H^+ + D_2$ ($v=0$, $j=0$), but the increasing trend of the RCT and the NRCT results over the investigated energy range also indicates that, at higher collision energies, the nonadiabatic transition mechanism involving several potential energy surfaces may act and its contribution to the underlying mechanism increases slightly as the collision energy increases. The calculated results deriving from different initial states of D_2 molecule also provide an insight into the effects of the vibrational excitation and the rotational excitation on the reaction probabilities. The increase of the RCT and the NRCT probabilities with increasing initial vibrational quantum number v, verifies the important role of the vibrational excitation in the nonadiabatic transitions and also the fact that $v=4$ of D_2 is the most likely vibrational level to access the crossing seam. The rotational excitation has little effect on the RCT channel while it enhances the NRCT to some extent and mildly decreases the RNCT probabilities. It is also revealed that the vibrational excitation leads to more remarkable nonadiabatic transitions than the rotational excitation.

5. Conclusions

The time-dependent wave packet approach has been improved for the treatment of nonadiabatic problems, and the method is then applied to dynamics studies in a variety of triatomic reaction systems, such as the reactions over barriers, the reactions involving long-lived complex formation, and the ion–molecule collisions with charge transfer processes. These applications not only produce numerical results serving to interpret and to predict nonadiabatic features of chemical reactions, but also to demonstrate that the improved time-dependent quantum method is computational tractable and it may

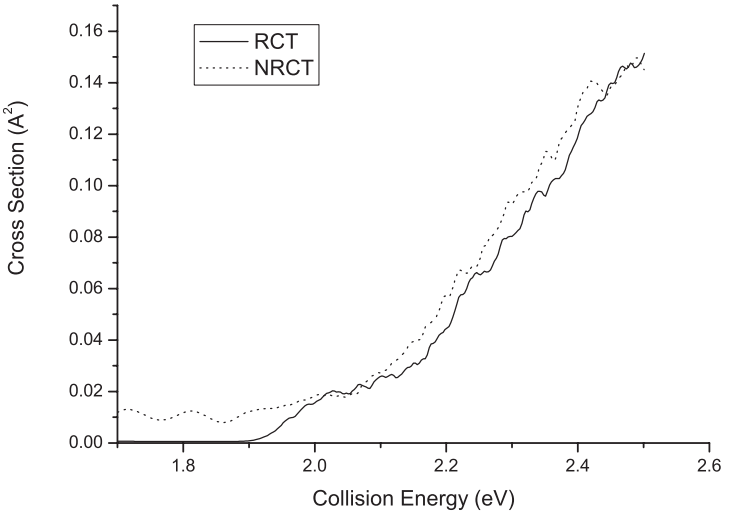

Figure 26. Comparison of cross sections between the RCT and the NRCT processes; taken from [10].

be a good method complement to the time-independent quantum approach for treating the nonadiabatic chemical processes, particularly for the study of nonadiabatic systems with deep wells where the quantum treatment assumes even further complexity due to the complex formation.

Although the computed total reaction cross sections with the present time-dependent wave packet method can be used for a direct comparison with experimental measurement, it is necessary to further develop this method to produce state-resolved quantum results such as the differential cross sections and the product state distributions for a more detailed comparison with experiments, due to the fact that the state-to-state differential cross sections have already been obtained experimentally for the triatomic and the larger chemical systems. In this regard, our work in progress includes the $F + H_2$ reaction [90]. This method needs to be modified and extended to the reactions with four or more atoms as well since the time-dependent wave packet method has been applied to a variety of triatomic systems thus far. But such quantum treatment of polyatomic systems is rather difficult partly due to the increasing computational cost and the lack of an accurate diabatic potential energy surface even for four-atom systems. It is thus emphasised that significant advances in the electronic structure theory and in the capacity of computers play a crucial role in the extension of the method to the polyatomic reactions.

In this review, we mainly concentrate on the applications to reactive scattering systems that vary widely in their dynamical behavior. However, it is possible to make this diversity expanded in applications to other processes. A similar idea can be used to describe the electron dynamics by solving the Schrödinger equation of electrons coupled with nuclei, and thus the time-dependent wave packet method can be extended to the frontier attosecond area where the attosecond technique is used to probe the electron dynamics that occurs within a time scale of attoseconds. In our recent work [91], we investigated the recollisions between an electron and D_2^+ ion and reproduced the experimentally measured kinetic energy spectra of D^+ ion using a similar

time-dependent wave packet method. Thus, the quantum physical picture for the entanglement between the electron and the nuclei are provided through the calculated recollision probabilities. The example of describing one electron dynamics has proved the feasibility of interpreting the molecular dynamics in attosecond time scale by using the time-dependent wave packet methodology, with more challenges coming from the attempt to describe the dynamics involving two or more electrons. Studies using the present time-dependent wave packet method could also be devoted to the unimolecular nonadiabatic processes, such as the cases in the resonance studies of $H + H_2$ [92] and $Cl + H_2$ [93] as well as in the photodissociation investigations [94]. Still, many other efforts have been devoted to the treatment associated with photodissociation dynamics [95, 96, 105–111], but these are quite beyond the scope of this review.

Acknowledgments

This work was supported by the Knowledge Innovation Program of the Chinese Academy of Sciences (INF105-SCE-02-08) and NSFC (20373071, 20333050, 20573110). The authors thank H. J. Werner, Aron Kuppermann, George Schatz, Peter Knowles, Hiroki Nakamura, and Shigeki Kato for providing them with the PESs and the spin–orbit matrix during the study.

References

[1] W. A. Jasper, C. Zhu, S. Nangia, and D. G. Truhlar, Faraday Discus. **127,** 1 (2004).
[2] J. C. Tully, Faraday Discuss. **127,** 463 (2004).
[3] A. Kuppermann and R. Abrol, Adv. Chem. Phys. **124,** 283 (2002).
[4] A. Toniolo, S. Olsen, L. Manohar, and T. J. Martinez, Faraday Discuss. **127,** 149 (2004).
[5] J. N. Harvey, Faraday Discuss. **127,** 165 (2004).
[6] A. Migani, A. Sinicropi, N. Ferrè, A. Cembran, M. Garavelli, and M. Olivucci, Faraday Discuss. **127,** 179 (2004).
[7] J. C. Tully, Dynamics of molecular collisions, Part B, Ed. W. H. Miller (Plenum, New York, 1976), pp. 217–267.
[8] J. C. Tully, J. Chem. Phys. **93,** 1061 (1990).
[9] A. W. Jasper, S. N. Stechmann, and D. G. Truhlar, J. Chem. Phys. **116,** 5424 (2002).
[10] A. W. Jasper, S. N. Stechmann, and D. G. Truhlar, J. Chem. Phys. **117,** 10427 (2002).
[11] M. Thachuk, M. Y. Ivanov, and D. M. Wardlaw, J. Chem. Phys. **109,** 5747 (1998).
[12] H. Wang, M. Thoss, and W. H. Miller, J. Chem. Phys. **115,** 2979 (2001).
[13] C. Zhu, S. Nangia, A. W. Jasper, and D. G. Truhlar, J. Chem. Phys. **121,** 7658 (2004).
[14] M. D. Hack, A. M. Wensmann, D. G. Truhlar, M. Ben-Nun, and T. J. Martinez, J. Chem. Phys. **115,** 1172 (2001).
[15] T. J. Martinez, M. Ben-Nun, and R. D. Levine, J. Phys. Chem. **100,** 7884 (1996).
[16] I. Burghardt, M. Nest, and G. A. Worth, J. Chem. Phys. **119,** 5364 (2003).
[17] G. A. Worth, M. A. Robb, and I. Burghardt, Faraday Discuss. **127,** 307 (2004).
[18] R. Kosloff, J. Phys. Chem. **92,** 2087 (1988).
[19] D. H. Zhang and J. Z. H. Zhang, in *Dynamics of Molecules and Chemical Reactions*, edited by R. E. Wyatt and J. Z. H. Zhang (Marcel Dekker, New York, 1996), Ch. 6 and references therein.
[20] D. H. Zhang and J. Z. H. Zhang, J. Chem. Phys. **101,** 1146 (1994).
[21] J. Z. H. Zhang, J. Dai, and W. Zhu, J. Phys. Chem. A **101,** 2746 (1997).
[22] D. Neuhauser, M. Baer, R. S. Judson, and D. J. Kouri, Comp. Phys. Comm. **63,** 460 (1991).
[23] S. C. Althorpe and D. C. Clary, Ann. Phys. Chem. **54,** 493, and references therein (2003).
[24] G. C. Schatz, J. Phys. Chem. **100,** 12839 (1996).
[25] J. C. Tully, J. Chem. Phys. **60,** 3042 (1974).
[26] F. Rebentrost and W. A. Lester Jr., J. Chem. Phys. **67,** 3367 (1977).
[27] R. E. Wyatt and R. B. Walker, J. Chem. Phys. **70,** 1501 (1979).

[28] G. D. Billing, L. Y. Rusin, and M. B. Sevryuk, J. Chem. Phys. **103,** 2482 (1995).
[29] M. Gilibert and M. Baer, J. Phys. Chem. **98,** 12822 (1994).
[30] M. H. Alexander and D. E. Manolopoulos, J. Chem. Phys. **109,** 5710 (1998).
[31] M. H. Alexander, D. E. Manolopoulos, and H. J. Werner, J. Chem. Phys. **113,** 11084 (2000).
[32] Y. R. Tzeng and M. H. Alexander, J. Chem. Phys. **121,** 5812 (2004).
[33] Y. R. Tzeng and M. H. Alexander, J. Chem. Phys. **121,** 5183 (2004).
[34] F. Dong, S.-H. Lee, and K. Liu, J. Chem. Phys **113,** 3633 (2000).
[35] W. B. Chapmann, B. W. Blackmon, and D. J. Nesbitt, J. Chem. Phys. **107,** 8193 (1997).
[36] D. M. Neumark, A. M. Wodtke, G. N. Robinson, C. C. Hayden, and Y. T. Lee, J. Chem. Phys. **82,** 3045 (1985).
[37] M. H. Alexander, G. Capecchi, and H. J. Werner, Faraday Discuss. **127,** 59 (2004).
[38] N. Balucani, D. Skouteris, G. Capozza, E. Segoloni, P. Casavecchia, M. H. Alexander, G. Capecchi, and H. J. Werner, Phys. Chem. Chem. Phys. **6,** 5007 (2004).
[39] N. Balucani, D. Skouteris, L. Cartechini, G. Capozza, E. Segoloni, P. Casavecchia, M. H. Alexander, G. Capecchi, and H. J. Werner, Phys. Rev. Letts. **91,** 013201 (2003).
[40] M. H. Alexander, E. J. Rackham, and D. E. Manolopoulos, J. Chem. Phys. **121,** 5221 (2004).
[41] D. Skouteris, A. Lagana, G. Capecchi, and H. Werner, Phys. Chem. Chem. Phys. **6,** 5000 (2004).
[42] T. X. Xie, Y. Zhang, and K. L. Han, Chinese J. Chem. Phys. **17,** 657 (2004).
[43] S. K. Gray and G. G. Balint-Kurti, J. Chem. Phys. **108,** 950 (1998).
[44] C. S. Maierle, G. C. Schatz, M. S. Gordon, *et al*., J. Chem. Soc. Faraday Trans. **93,** 709 (1997).
[45] A. J. Dobbyn, J. N. L. Connor, N.A. Besley, P. J. Knowles, and G. C. Schatz, Phys. Chem. Chem. Phys. **1,** 957 (1999).
[46] T. W. J. Whiteley, A. J. Dobbyn, J. N. L. Connor, and G. C. Schatz, Phys. Chem. Chem. Phys. **2,** 549 (2000).
[47] G. C. Schatz, M. Hankel, T. W. J. Whiteley, *et al*., J. Phys. Chem. A **107,** 7278 (2003).
[48] M. Hankel, J. N. L. Connor, and G. C. Schatz, Chem. Phys. **308,** 225 (2005).
[49] G. C. Schatz, A. Papaioannou, L. A. Pederson, *et al*., J. Chem. Phys. **107,** 2340 (1997).
[50] G. C. Schatz, L. A. Pederson, and P. J. Kuntz, Faraday Discuss. **108,** 357 (1997).
[51] K. Drukker and G. C. Schatz, J. Chem. Phys. **111,** 2451 (1999).
[52] S. K. Gray, C. Petrongolo, K. Drukker, *et al*., J. Phys. Chem. **103,** 9448 (1999).
[53] S. K. Gray, G. G. Balint-Kurti, G. C. Schatz, J. J. Lin, X. H. Liu, S. Harich, and X. M. Yang, J. Chem. Phys. **113,** 7330 (2000).
[54] T. Takayanagi, J. Chem. Phys. **116,** 2439 (2002).
[55] M. R. Hoffmann and G. C. Schatz, J. Chem. Phys. **113,** 9456 (2000).
[56] B. Maiti and G. C. Schatz, J. Chem. Phys. **119,** 12360 (2003).
[57] B. Maiti, G. C. Schatz, and G. Lendvay, J. Phys. Chem. A **108,** 8772 (2004).
[58] L. A. Pederson, G. C. Schatz, T. Hollebeek, *et al*., J. Phys. Chem. A **104,** 2301 (2000).
[59] F. Santoro, C. Petrongolo, and G. C. Schatz, J. Phys. Chem. A **106,** 8276 (2002).
[60] G. C. Schatz, B. Fisher, W. Grande, *et al*., J. Phys. Chem. A **105,** 2515 (2001).
[61] J. C. Tully and R. K. Preston, J. Chem. Phys. **55,** 562 (1972).
[62] C. Y. Zhu, H. Kamisaka, and H. Nakamura, J. Chem. Phys. **116,** 3234 (2002).
[63] C. Y. Zhu, H. Kamisaka, and H. Nakamura, J. Chem. Phys. **115,** 11036 (2001).
[64] H. Kamisaka, W. Bian, K. Nobusada, and H. Nakamura, J. Chem. Phys. **116,** 654 (2002).
[65] T. Takayanagi, Y. Kurosaki, and A. Ichihara, J. Chem. Phys. **112,** 2615 (2000).
[66] V. G. Ushakov, K. Nobusada, and V. I. Osherov, Phys. Chem. Chem. Phys. **3,** 63 (2001).
[67] A. Ichihara, O. Iwamoto, and R. K. Janev, J. Phys. B **33,** 4747 (2000).
[68] M. Chajia and R. D. Levine, Phys. Chem. Chem. Phys. **1,** 1205 (1999).
[69] A. Ichihara, T. Shirai, and K. Yokoyama, J. Chem. Phys. **105,** 1857 (1996).
[70] T. Takayanagi, J. Phys. Chem. A **106,** 4914 (2002).
[71] G. E. Zahr, R. K. Preston, and W. H. Miller, J. Chem. Phys. **62,** 1127 (1975).
[72] H. Tachikawa, T. Hamabayashi, and H. Yoshida, J. Phys. Chem. **99,** 16630 (1995).
[73] T. Takayanagi and Y. Kurosaki, J. Chem. Phys. **113,** 7158 (2000).
[74] M. Sizun, J. B. Song, and E. A. Gislason, J. Chem. Phys. **109,** 4815 (1998).
[75] M. Sizun, J. B. Song, and E. A. Gislason, J. Chem. Phys. **116,** 2888 (2002).
[76] P. Halvick, M. Boggio-Pasqua, L. Bonnet, *et al*., Phys. Chem. Chem. Phys. **4,** 2560 (2002).
[77] M. Jungen, M. Lehner, R. Guerout, *et al*., Phys. Chem. Chem. Phys. **6,** 1666 (2004).
[78] J. A. Fleck Jr., J. R. Morris, and M. D. Feit, Appl. Phys. **10,** 129 (1976).
[79] M. Born and K. Huang, *Dynamical theory of crystal Lattices* (Oxford University Press, New York, 1954).
[80] M. Faubel, B. Martınez-Haya, L. Y. Rusin, U. Tappe, and J. P. Toennies, J. Chem. Phys. A **101,** 6415 (1997).
[81] R. T. Skodje, D. Skouteris, D. E. Manolopoulos, S.-H. Lee, F. Dong, and K. Liu, J. Chem. Phys. **112,** 4536 (2000).

[82] Y. Matsumi and A. M. S. Chowdhury, J. Chem. Phys. **104,** 7036 (1996).
[83] H. Nakamura and S. Kato, J. Chem. Phys. **110,** 9937 (1999).
[84] S. Rogers, D. Wang, A. Kuppermann, and S. Walch, J. Phys. Chem. A **104,** 2308 (2000).
[85] J. Dobbyn and P. J. Knowles, Faraday Discuss. **110,** 247 (1998).
[86] M. Braunstein, S. Adler-Golden, B. Maiti, and G. C. Schatx, J. Chem. Phys. **120,** 4316 (2004).
[87] N. Balakrishnan, J. Chem. Phys. **121,** 6346 (2004).
[88] C. Schlier, U. Nowotny, and E. Teloy, Chem. Phys. **111,** 351 (1987).
[89] G. Ochs and E. Teloy, J. Chem. Phys. **61,** 4930 (1974).
[90] Y. Zhang, T. X. Xie, K. L. Han, and J. Z. H. Zhang, J. Chem. Phys. **124,** 134301.
[91] J. Hu, K. L. Han, and G. Z. He, Phys. Rev. Lett. **95,** 123001 (2005).
[92] A. J. C. Varandas and H. G. Yu, Chem. Phys. Lett. **259,** 336 (1996).
[93] S. Ghosal and S. Mahapatra, J. Phys. Chem. A **109,** 1530 (2005).
[94] M. Y. Zhao, Q. T. Meng, T. X. Xie, K. L. Han, and G. Z. He, Int. J. Quantum Chem. **101,** 153 (2005).
[95] A. Brown and G. G. Balint-Kurti, J. Chem. Phys. **113,** 1870 (2000).
[96] A. Brown and G. G. Balint-Kurti, J. Chem. Phys. **113,** 1879 (2000).
[97] Y. Zhang, T. X. Xie, K. L. Han, and J. Z. H. Zhang, J. Chem. Phys. **119,** 12921 (2003).
[98] Y. Zhang, T. X. Xie, and K. L. Han, J. Phys. Chem. A **107,** 10893 (2003).
[99] Y. Zhang, T. X. Xie, and K. L. Han, J. Chem. Phys. **120,** 6000 (2004).
[100] T. X. Xie, Y. Zhang, and K. L. Han, Chem. Phys. Lett. **398,** 313 (2004).
[101] T. S. Chu, T. X. Xie, and K. L. Han, J. Chem. Phys. **121,** 9352 (2004).
[102] T. S. Chu, X. Zhang, and K. L. Han, J. Chem. Phys. **122,** 214301 (2005).
[103] T. S. Chu and K. L. Han, J. Phys. Chem. A **109,** 2050 (2005).
[104] R. F. Lu, T. S. Chu, and K. L. Han, J. Phys. Chem. A **109,** 6683 (2005).
[105] H. Guo and G. C. Schatz, J. Chem. Phys. **93,** 393 (1990).
[106] H. Guo and G. C. Schatz, J. Phys. Chem. **95,** 3091 (1991).
[107] H. Guo, J. Chem. Phys. **96,** 6629 (1992).
[108] B. Heumann, K. Weide, R. Duren, and R. Schinke, J. Chem. Phys. **98,** 5508 (1993).
[109] D. Simah, B. Hartke, and H.-J. Werner, J. Chem. Phys. **111,** 4523 (1999).
[110] H. Flothmann, C. Beck, R. Schinke, C. Woywod, and W. Domcke, J. Chem. Phys. **107,** 7296 (1997).
[111] H. Flothmann, R. Schinke, C. Woywod, and W. Domcke, J. Chem. Phys. **109,** 2680 (1998).